Joint Remote Laser Induced Breakdown Spectroscopy and Raman Laser Spectroscopy for Investigation of Planetary Geochemical Composition

Mahider Kebede Tessema

A Thesis Submitted to Department of Applied Physics, School of Applied Natural Sciences

Presented in Partial Fulfillment of the Requirement for the Degree of Masters of Science in Applied Physics (Laser Spectroscopy)

Office of Graduate Studies

Adama Science and Technology University

June, 2024

Adama, Ethiopia

Joint Remote Laser Induced Breakdown Spectroscopy and Raman Laser Spectroscopy for Investigation of Planetary Geochemical Composition

Mahider Kebede Tessema

Advisor: Dr. Alemu Kebede Hordofa

A Thesis Submitted to Department of Applied Physics, School of Applied Natural Sciences

Presented in Partial Fulfillment of the Requirement for the Degree of Masters of Science in Applied Physics (Laser Spectroscopy)

Office of Graduate Studies

Adama Science and Technology University

June, 2024

Adama, Ethiopia

Declaration

I hereby declare that this Master thesis entitled "**Joint Remote Laser Induced Breakdown Spectroscopy and Raman Laser Spectroscopy for Investigation of Planetary Geochemical Composition**" is my original work. That it has not been submitted for the award of any academic degree, diploma or certificate in any other university. All sources of materials that are used for this thesis have been duly acknowledged through citation.

Name: Mahider Kebede Tessema

Signature: _____

Recommendation

I, the advisor of this thesis, hereby certify that I have read the revised version of the thesis entitled "**Joint Remote Laser Induced Breakdown Spectroscopy and Raman Laser Spectroscopy for Investigation of Planetary Geochemical Composition**" Prepared under our guidance by Mahider Kebede Tessema submitted in partial fulfillment of the requirement for the degree of Masters of Science in Applied Physics. Therefore, I recommend that the submission of the revised version of the Thesis to the department following the applicable procedures.

_____	_____	_____
Name of Advisor	Signature	Date

Approval Board of Examiners

We, the underlined, members of the Board of Examiners of the thesis by Mahider Kebede Tessema have read and evaluated the thesis entitled "**Joint Remote Laser Induced Breakdown Spectroscopy and Raman Laser Spectroscopy for Investigation of Planetary Geochemical Composition**" and examined the candidate during open defense. This is, therefore, to certify that the thesis is accepted for partial fulfilment of the requirement of the degree of Master of Science in Applied Physics (Laser Spectroscopy).

Chairperson	Signature	Date
Internal Examiner	Signature	Date
External Examiner	Signature	Date

Final approval and acceptance of the thesis is contingent upon submission of its final copy to the Office of Postgraduate Studies (OPGS) through the Department Graduate Council (DGC) and School Graduate Committee (SGC).

Department Head	Signature	Date
School Dean	Signature	Date
Office of Postgraduate Studies, Dean	Signature	Date

ACKNOWLEDGMENTS

First and foremost, I would like to thank God, who gave me everlasting life that was ransom for all. Next, I would like to express my deepest gratitude to my advisor Assoc. Pro. Alemu Kebede Hordofa for his expert guidance, constructive comments, suggestions and encouragement throughout my study period. I also extend my sincere Thanks to the staff of physics department.

Finally, I am deeply grateful to my family and my friends, especially to my parents for their support and understanding.

List of Acronyms and Abbreviations

ICA	Independent component analysis
LDA	Linear discriminate analysis
LIBS	Laser-induced breakdown spectroscopy
LTE	Local thermodynamic equilibrium
LVs	Latent variables
MVA	Multivariate data analysis
NASA's	National aeronautics and space administration’s
NIST	National Institute of Standards and Technology
Nd:YAG	Neodymium-doped yttrium aluminum garnet
PC	Principal Component
PCA	Principal Component analysis
PLS-R	Partial least-squares regression
RLS	Raman laser spectrometer
RRUFF	Raman Raman User Friendly Field Frequency
TE	Thermodynamic equation
UV	Ultraviolet
VIS	Visible

Table of Contents

List of Table

List of Figures

ABSTRACT

This thesis focuses on combining Raman spectroscopy and LIBS for planetary geochemical investigations, specifically targeting minerals commonly found in extraterrestrial environments: chalcanthite, calcite, halite, olivine, gypsum, nontronite, and quartz. Spectral datasets for these minerals were obtained from the Raman Raman User Friendly Field Frequency (RRUFF) database, and the elemental Compositions of minerals such as $CuSO_4 \cdot 5H_2O$, $CaCO_3$, NaCl, Fe_2SiO_4, Mg_2SiO_4, $CaSO_4 \cdot 2H_2O$, $Na_{0.3}Fe^{3+}_2(Si,Al)_4O_{10}(OH)_2 \cdot nH_2O$ and SiO_2 were sourced from the National Institute of Standards and Technology (NIST) database and imported into Origin software. After preprocessing steps in Origin, including baseline correction and noise reduction, the spectral data were combined using fusion. When combined, these techniques provide complementary data, raising the question of how to optimize their use to maximize scientific output. To address this question, we conducted a study in which we investigated LIBS and Raman data, their mixtures, multivariate data analysis (MVA) techniques and specifically principal component analysis (PCA) to assess the potential of identifying targeting minerals commonly found in extraterrestrial environments using LIBS and Raman data alone, as well as their fused data. Our findings indicate that data fusion of LIBS and Raman spectroscopy enhanced the detection capabilities compared to individual techniques, this fusion approach reveals new aspects that would remain hidden if the data were not integrated, highlighting the benefits of a combined analysis.

Keywords:

Raman spectroscopy, LIBS, planetary geochemical, data fusion

CHAPTER ONE

1. INTRODUCTION

1.1 Background of the Study

Planetary geochemical investigation involves studying the elemental composition and mineralogical characteristics of planetary surfaces to understand their geological history, formation processes, and potential for habitability. Before the advent of laser-induced breakdown spectroscopy (LIBS) and Raman spectroscopy techniques, planetary geochemical investigations were primarily conducted through visual observation, sample collection, and remote sensing techniques such as infrared spectroscopy and X-ray fluorescence (Pieters and Englert, 1993).

Visual observation involved analyzing images of planetary surfaces taken by orbiters or rovers to identify geological features and potential areas of interest for sample collection. Sample collection missions, such as the Apollo missions to the Moon, involved astronauts collecting rock and soil samples for analysis on Earth. These samples provided direct information about the mineralogy and geochemistry of planetary materials (Wilhelms, 1993).

Remote sensing techniques, such as infrared spectroscopy and X-ray fluorescence, allowed researchers to analyze the composition of planetary surfaces from a distance. Infrared spectroscopy measured the absorption and emission of infrared light by minerals to identify their composition, while X-ray fluorescence measured the fluorescent X-rays emitted by elements in a sample to determine their elemental composition. However, these traditional methods had limitations in terms of sample collection, analysis time, and spatial resolution. With the development of LIBS and Raman spectroscopy techniques, planetary geochemical investigations have become more efficient and effective. LIBS enable rapid multi-elemental analysis by ablating material from the sample with a laser and analyzing the resulting plasma emission spectroscopic (Cremers and Radziemski, 2006). Raman spectroscopy, on the other hand, is a non-destructive method that detects the vibrational and rotational states of molecules to determine the mineralogy and molecular structure of samples (Kerr, 1959).

Spectroscopy is one of the most powerful scientific tools for studying nature. The study of celestial bodies using spectroscopy connects astronomy with fundamental physics at atomic and molecular levels (Clark, 1999).

Currently, laser induced breakdown spectroscopy (LIBS) is becoming increasingly acceptable as an important tool in astronomy. In the LIBS technique, powerful laser pulses of >1 GW/cm2 peak power are focused on a targeted sample to form a plasma. The laser-induced plasma contains electronically excited atoms, ions, and molecules of the sample. These excited species emit radiations characteristic of the material ingredients of the sample via their unique spectral autographs. The light from the plasma can be detected and analyzed at a particular delay time after the formation of plasma. Because there's no laborious sample preparation required, LIBS has demonstrated its potential applications in qualitative analysis and quantitative determination of elemental composition of various samples even in hostile environments (Singh and Thakur, 2007).

The field of LIBS has shown remarkable expansion in the past few years. The spectral lines emitted from the plasma light can be detected, recorded, and analyzed at a certain time delay after the initiation of the laser spark. In addition to its use as an elemental detector, LIBS is being developed for other potential applications through combination with Raman spectroscopy (Boss and Fredeen 1997). As a nondestructive technique, Raman spectroscopy is one of the most attractive analytical methods and is based on scattering monochromatic light and detecting sidebands due to an exchange of energy between the light and analytic molecules. Thus, the combination of LIBS and Raman could give comprehensive information on an unknown sample, including not only its elemental composition but also the molecular configuration (Gaft, Nagli and Modiano, 2005). In brief, the LIBS technique is well known to have better sensitivity in detecting metal than nonmetals elements. In addition, it has better response to cations other than anionic species. This insufficiency can be well compensated for by adding the function of Raman spectroscopy, which can identify the anion groups in crystals and crystal forms from Raman-active lattice modes (Smith and Dent, 2005). Similarly, inorganic composites give well-defined Raman bands in their spectra, which are well resolved from those frequencies (Raman shift) of the organic groups (Long, 2002). Therefore, it would be easy to use both techniques ways together to achieve the discrimination between inorganic and organic compounds. Hence, the combined technique is shown to be a more important analytical tool than its individual components.

Although a few published papers have explored aspects of this hybrid technique, to the best of our knowledge there is less general overview of this hybrid technique in the past few years (Harmon, Russo and Hark, 2013). The goal of this research is identification and analysis of mineral compositions by leveraging the combined use of Laser-Induced Breakdown Spectroscopy (LIBS) and Raman spectroscopy.

The thesis is organized in four chapters. This Introductory chapter consists of background of the study, statement of the problem, objectives of the study, beneficiary of the study and significant of the study. The second chapter describes literature reviews that were given by different researchers. The third chapter discusses methods and materials; which contains study area, data source and software used during data collection and analysis. The fourth chapter shows the result and discussion, conclusion and recommendation of this study.

1.2 Statement of the Problem

Both LIBS and Raman Spectroscopy are primarily surface analytical techniques. Research efforts are needed to enhance their capabilities for depth profiling and subsurface analysis of planetary materials. Developing methods that allow these techniques to probe deeper into geological samples or penetrate regolith layers on planetary surfaces could provide more comprehensive insights into the composition and structure of celestial bodies.

Improving the accuracy and precision of quantitative analysis using LIBS and Raman Spectroscopy remains a significant challenge. Establishing robust calibration methods and standards for quantification of elements and compounds on different planetary surfaces is essential for reliable and consistent data interpretation. Addressing these research gaps will contribute significantly to advancing the effectiveness, reliability, and applicability of Laser-Induced Breakdown Spectroscopy (LIBS) and Raman Spectroscopy in planetary geochemical analysis, enabling deeper insights into the composition, history, and potential habitability of celestial bodies beyond Earth.

Research questions

- Can LIBS and Raman spectroscopy be utilized for remote or in-situ planetary exploration?
- Does LIBS and Raman spectroscopy provide rapid elemental analysis of elemental compositions within planetary materials?
- Can Remote Laser-Induced Breakdown Spectroscopy (LIBS) and Raman Laser Spectroscopy play pivotal roles in investigating planetary bodies?

1.3 Objective of the Study

1.3.1 General Objective

The general objective of this study is to investigate Joint geochemical composition in the planetary surface using remote Laser induced breakdown spectroscopy and Raman spectroscopy techniques.

1.3.2 Specific Objective

The specific objective of this thesis is

- To analysis elemental and molecular compositions using combined LIBS and Raman spectroscopy within planetary materials.
- To identify the joint spectra and several relevant peaks of minerals using Raman spectroscopy and LIBS.
- To detect elements or minerals critical for characterizing extraterrestrial geological formations,
- To visualize high dimensional data particularly within Principal Component Analysis (PCA).
- To compare the geochemical factors analyzed through Raman spectroscopy and Laser Induced Breakdown Spectroscopy (LIBS) for a comprehensive understanding of planetary surface compositions.

1.4 Beneficiary of the Study

The results of this study will benefit a wide range of stakeholders, including:

- The study will provide valuable educational resources for those interested in planetary science, spectroscopy, and astrobiology, enhancing their knowledge and understanding of these fields.
- The evidence presented regarding planetary surface compositions and related issues will aid geologists and space explorers in their research and exploratory missions.
- Insights into the capabilities of Laser-Induced Breakdown Spectroscopy (LIBS) and Raman Spectroscopy will inform researchers, facilitating better analytical techniques in planetary geochemical analysis.
- Organizations involved in space exploration will benefit from the study's findings, which highlight the advantages of using LIBS and Raman Spectroscopy in analyzing planetary surfaces.

The study's implications for understanding planetary compositions will be particularly valuable for astrobiologists seeking to identify signs of life beyond Earth.

1.5 Significance of the Study

The result of this thesis gives an idea about Laser-Induced Breakdown Spectroscopy (LIBS) and Raman Spectroscopy are invaluable tools for planetary geochemical analysis, offering non-destructive, rapid and informative methods for studying the compositions and characteristics of planetary surfaces, thereby contributing significantly to our understanding of other celestial bodies in the planetary system and beyond. Hence, the findings and recommendations will aid in the search for life and understanding planetary compositions.

The result of this study:

- Serve as valuable educational resources for students, researchers, and educators interested in planetary science, spectroscopy, and astrobiology.
- Gives evidence for geologists, space explores about composition and related issues on planetary surface.
- Gives insights for scientific community and researcher regarding the capabilities of Laser-Induced Breakdown Spectroscopy (LIBS) and Raman Spectroscopy.

Overall, the findings from this thesis, highlighting the benefits of LIBS and Raman Spectroscopy in planetary geochemical analysis, will have a wide-reaching impact on space exploration, scientific knowledge and the pursuit of understanding planetary compositions and potential habitats for life in the universe. The basic principles of Laser-Induced Breakdown Spectroscopy (LIBS) and Raman Laser Spectroscopy and their applications on Astrophysics through interpretation of LIBS and Raman data using the suitable software Origin to show Astro spectroscopic technique is really essential for the development of space exploration.

CHAPTER TWO

2. LITERATURE REVIEW

2.1 Theory of LIBS and Raman spectroscopy

Since the invention and ongoing development of lasers starting in the 1960s, LIBS and Raman spectroscopy have found an increasing number of applications across diverse fields, including the steel and nuclear industries, medical applications, and cultural heritage preservation (Hahn and Omenetto, 2010). Moreover, both techniques have been extensively proposed for in-situ exploration of extraterrestrial bodies (Colao et al, 2004). Their capability for remote measurements without the need for sample preparation is a significant advantage, making them particularly suitable for analyzing the surfaces of planetary bodies.

2.1.1 Laser induced breakdown spectroscopy process

The interaction of lasers with matter invariably involves an exchange of energy. When a laser beam is directed at a dense material, the laser energy can be scattered at the same wavelength, reemitted at different wavelengths, absorbed or transmitted through the sample. This interaction can lead to partial evaporation, initiating a process known as laser-induced ablation.

Laser Induced Breakdown Spectroscopy (LIBS) is a simultaneous multi elemental analysis technique based on this principle. A pulsed laser beam is focused on the sample surface, generating plasma that atomizes and excites the ablated material. When the laser irradiance exceeds approximately 1 GW/cm² (Senesi, 2014), mass is ablated, evolving into plasma. This plasma comprises electrons, excited atoms, ions, and simple molecules that emit characteristic radiation. The energy released from these excited species generates emission spectra with distinct lines representing each element in the sample. As illustrated in Fig.1 tightly focusing the radiation from a rapidly pulsed laser onto a material's surface causes heating, ablation, vaporization, and plasma formation. Within the hot plasma, atoms and ions are excited, and photons are emitted due to specific atomic or ionic transitions and ion recombination during plasma cooling. This emitted light can be analyzed spectroscopic to obtain a comprehensive chemical signature, or geochemical fingerprint, with typical elemental detection limits of tens of ppm or lower. Spectral analysis of this radiation

provides spectra over a wide range, from UV to NIR, with elemental emission lines and a few molecular emission bands (Cremers and Radziemski, 2013).

In recent years, LIBS has found applications across many research areas due to its multi-elemental capabilities, high acquisition rate (up to 1000 spectra per second), compatibility with optical microscopy, and sensitivity from major components to trace elements (very high sensitivity for various elements) (Hahn and Omenetto, 2010).An advantage of LIBS imaging platforms is the ease of integrating other spectroscopic techniques using the same microscope to provide multimodal images (Surmick, Leahy-Hoppa and Malenfant, 2016). The previous work, demonstrated the potential of data fusion between LIBS and Plasma Induced Luminescence for better interpretation of complex spectral signatures (Clegg, Wiens, Maurice and Bousquet, 2009).

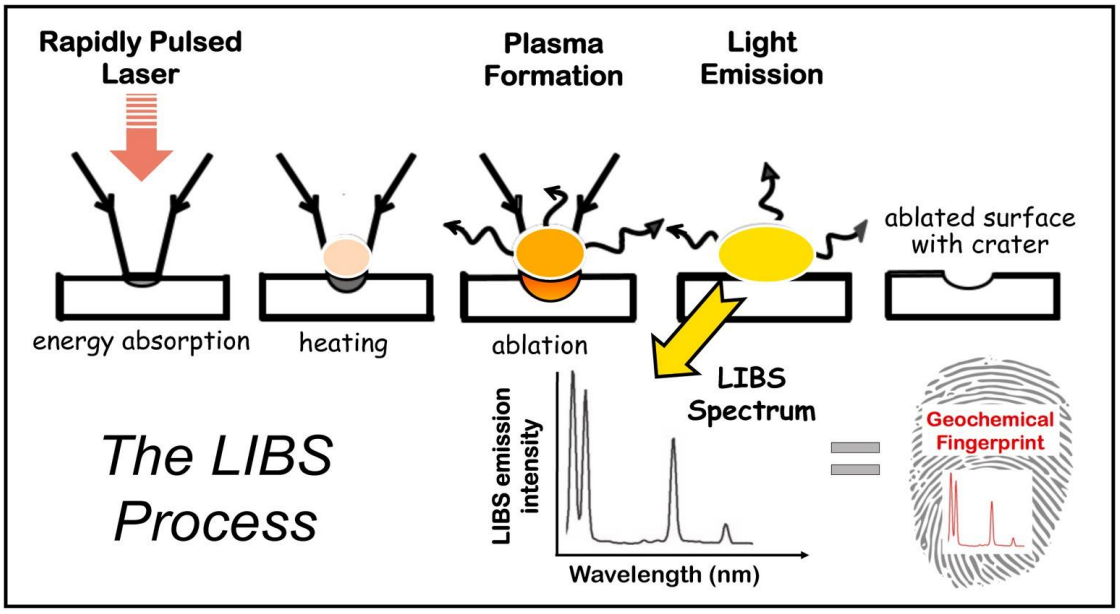

Figure 1: LIBS process for multi-elemental analysis.

Attributes of LIBS for Geochemical Analysis

LIBS possess several attributes that make it a highly effective tool for analyzing geological and environmental materials, including:

- LIBS can provide real time chemical analysis in less than one second.
- It captures the full elemental composition of a sample with a single laser pulse, as every element in the periodic table has one or more emission lines in the ultraviolet, violet, visible, and near-infrared spectral regions (200-900 nm).

- LIBS are particularly sensitive to light elements like H, Li, Be, B, and C, which many other analytical methods struggle to detect.
- It requires only pictograms (pg) to nanograms (ng) of material for analysis.
- LIBS can perform compositional profiling to depths greater than 100 μm.
- It enables in situ analysis of individual particles, mineral grains, and both liquid and solid inclusions.
- LIBS can be used in the field with little to no sample preparation, although laboratory use for specific applications can benefit from careful preparation.
- The system comprises only a few relatively simple components (laser, optics, detector/spectrograph, and computer).

These attributes make LIBS suitable for a wide range of applications, from laboratory analyses to stand-off analyses where the sample is at a distance from the system, and for the development of portable and handheld analyzers. Laser-Induced Breakdown Spectroscopy (LIBS) instrumentation is generally less expensive and has lower operational costs than many other analytical techniques due to several factors. The setup of LIBS instruments is relatively simple, comprising mainly a laser source, focusing optics, and a spectrometer. This straightforward design reduces both manufacturing and maintenance expenses. Additionally, LIBS requires minimal to no sample preparation, which cuts down on the time and resources needed for analysis, in contrast to techniques like X-ray diffraction or electron microscopy that often necessitate extensive sample preparation. The versatility and portability of LIBS instruments allow for in-situ measurements in various environments, reducing the need for costly, specialized laboratory facilities. Moreover, LIBS do not heavily depend on consumables such as reagents or gases, unlike methods such as gas chromatography or mass spectrometry, which helps in lowering ongoing operational costs. The ability of LIBS to provide rapid, real-time analysis increases efficiency and decreases the overall cost per analysis compared to more time-consuming methods. These factors collectively contribute to the cost-effectiveness of LIBS, making it an attractive option for applications including planetary (Hilbk-Kortenbruck et al., 2001).

2.1.2 Raman spectroscopy process

When energy is put into a system, the energy can be absorbed, remitted, scattered, reflected etc. Spectroscopy deals with the measurement and interpretation of electromagnetic radiation that is absorbed scattered or emitted by atoms, molecules or other chemical species (Hollas, J. M. 2004).

When light passes through a transparent medium, some of it is scattered in all directions. This scattering may be due to inhomogeneities, or small particles suspended in the medium Tyndall Effect (Tyndall, J. 1869), but it occurs also in homogeneous media where it is due to the molecules themselves. The classical theory of molecular scattering was proposed by Lord Rayleigh (Rayleigh, L. 1899).

Rayleigh scattering is due to the production in the molecule of an electric dipole vibrating with the period of the incident light and therefore the emitted light has the same frequency as the incident light. The emitted photon has the same wavelength ($\overline{\upsilon_0} = \frac{1}{\lambda_0}$) as the absorbing photon. Scattering of a $\lambda >$ particle size is in accordance with the Stoke's formula, viz.,

$$\text{Intensity, } \quad \boldsymbol{I} \propto \frac{\mathbf{1}}{\boldsymbol{\lambda^4}} \qquad (2.1)$$

Raman scattering finds its origins in Planck and Einstein's formulation ($E = \hbar\omega$) that light is not only wavelike in nature but has the dual character of waves and particles. Once scientists began thinking about the concept of light as particles, the possibility of inelastic scattering of these particles became a method of proof of this new theory (Raman, C. V., and Krishnan, K. S., 1928). Raman spectroscopy involves an inelastic scattering process where the energy of the scattered photon is either increased (anti-Stokes) or decreased (Stokes). The energy shift is small and can be attributed to absorbed or induced molecular or lattice vibrations (phonons). The Raman scattered radiation produces characteristic spectra relative to the excitation laser line. Unlike elastic scattering without energy transfer (Rayleigh scattering), Raman scattering is weak: only one in 10^6 scattered photons experience an energy shift due to the Raman Effect (Dubessy et al., 2012). Consequently, Raman spectrometers require high sensitivity, and narrow optical filters must be used to suppress Rayleigh scattered photons.

Figure 2 illustrates Raman scattering processes (Stokes and anti-Stokes) compared to other interactions between radiation and molecules. While infrared absorption and fluorescence involve really electronic or vibrational states, Rayleigh, Stokes, and anti-Stokes scattering involve virtual states (McCreery, 2000).

In Rayleigh scattering, the energy level remains the same as before the excitation of the virtual state. For Stokes scattering, the excited virtual state decays into a state with higher energy than before the excitation, resulting in the emission of a photon with less energy. In anti-Stokes scattering, the system starts in a higher energy state before excitation and transitions to a lower energy state after the decay of the virtual state, accompanied by the emission of a photon with increased energy (Ferraro, J. R., Nakamoto, K., & Brown, C. W. 2003).

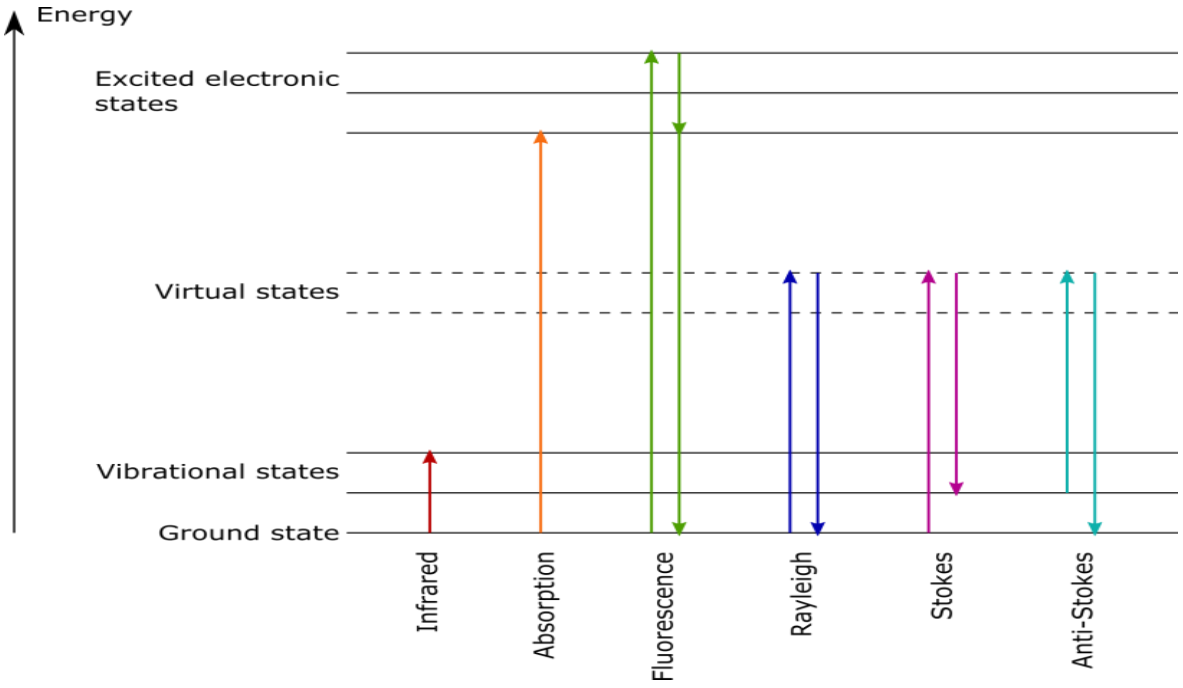

Figure 2: The processes of Raman scattering (Stokes and anti-Stokes)

Stokes and Anti-Stokes Equations

The intensity of the Raman-scattered light (both Stokes and anti-Stokes) depends on several factors including the frequency of the incident light, the molecular vibrations, and the Raman scattering cross-section of the molecule. The equations describing the intensities of Stokes and anti-Stokes lines generally involve terms related to the incident light frequency, the

Boltzmann factor (for thermal population of molecular states), and the Raman scattering cross-section (Pieters, C. M., & Englert, P. A. J., 1993).

Mathematically, the equations for the intensity of the Stokes (I-S) and anti-Stokes (I-AS) lines can be represented as:

$$I_S \propto \frac{1}{1-e^{-\frac{hc}{\lambda \kappa_B T}}} \tag{2.2}$$

$$I_{AS} \propto \frac{e^{-\frac{hc}{\lambda \kappa_B T}}}{1-e^{-\frac{hc}{\lambda \kappa_B T}}} \tag{2.3}$$

where: h is Planck's constant, c is the speed of light, λ is the wavelength of the incident light, κ_B is Boltzmann's constant, T is the temperature. These equations illustrate the relative intensities of Stokes and anti-Stokes lines depending on the temperature (through the Boltzmann factor) and the wavelength of the incident light (McCreery, R. L., 2000).

2.1.3 Combining LIBS and Raman spectroscopy

The combination of LIBS and Raman spectroscopy was implemented for several terrestrial studies and led, for example, to improved identification capabilities of inks or explosives. Also, for extraterrestrial applications, combined LIBS and Raman spectroscopy instruments were proposed with the Super Cam instrument on NASA's Mars 2020 mission, the first combined LIBS and Raman instrument for space exploration will be send to Mars (Wiens et al., 2017).

Regarding the hardware of a combined instrument, the two techniques can share some components as both need a laser, a spectrometer, and focusing and collection optics. For example, Super Cam has like Chem Cam three spectrometers from which the VNIR spectral range will be shared for both LIBS and Raman signal detection. Furthermore, the Super Cam laser which is a Nd:YAG laser can be used for both types of excitations: With its fundamental wavelength (1064 nm) it will create LIBS plasmas and due to frequency doubling its second harmonic mode at 532 nm will be used for time-resolved Raman spectroscopy (Wiens et al., 2017).

Not only is the possibility of sharing hardware components a reason for joint analysis, moreover, the data is highly complementary. LIBS data yields information of elemental

compositions of targets having a particular sensitivity to cationic elements, such as alkali and earth alkali metals. Although LIBS is generally capable of detecting all elements, it is challengedwith ionic elements such as halogens which have low signal intensities in the commonly used spectral ranges (200-900 nm). Raman spectroscopy, on the other hand, measures molecular and lattice vibrations that are mostly influenced by an ionic group such as the silicate or sulfate anion. In contrast to LIBS, cations can often only be detected indirectly with Raman spectroscopy via small shifts of anionic Raman modes depending on the kind of cation (Sharma, S. K., Misra, A. K., and Lucey, P. G. 2006).

Furthermore, LIBS and Raman spectroscopy provide a similar capability that qualifies them for robotic exploration of extraterrestrial bodies. These are in particular short measurement times (seconds to minutes) and the capability to measure remotely at distances varying from centimeters up to several meters. However, for remote Raman spectroscopy, dust covering the surface can impede the measurements. With combined LIBS and Raman instruments such as Super Cam, this problem can be overcome by removing dust with the shock wave of LIBS plasmas prior to Raman measurements. However, the laser matter interaction and the shock wave of LIBS measurements can alter the surface including the formation of newmolecules (Schröder, S., and Wiens, R. C. 2019).

2.2 Data Fusion

Data fusion, the process of combining information from multiple sources to improve decision-making, has gained significant attention across various scientific disciplines. In the realm of spectroscopic analysis, data fusion has emerged as a powerful tool for enhancing the accuracy and reliability of mineralogical studies and space exploration research. The importance of integrating information from different sources to derive comprehensive insights and facilitate informed decision-making processes (Gaft, M., Nagli, L., and Panczer, G. 2012).

In terrestrial studies, the fusion of Laser-Induced Breakdown Spectroscopy (LIBS) and Raman spectroscopy data has garnered considerable interest. Researchers have explored this approach for a range of applications, including the identification of inks, explosives, and geological fluids. By combining the elemental analysis capabilities of LIBS with the molecular identification capabilities of Raman spectroscopy, researchers have achieved enhanced accuracy and specificity in material characterization (Hoehse, 2012).

Moreover, recent advancements have extended the application of LIBS and Raman data fusion to space exploration endeavors. Moros et al. (2018) present a pioneering study wherein simultaneously collected LIBS and Raman data are utilized for mineral identification on Mars. Their approach involves a stepwise decision chain, wherein the cation component is first identified using LIBS, followed by comparison with stored Raman spectra of minerals containing the identified cation. This high-level data fusion strategy demonstrates the potential of integrating spectroscopic techniques for planetary exploration.

However, while existing studies have provided valuable insights into the fusion of LIBS and Raman data, there remains a need to further explore and refine these methodologies. Specifically, there is a dearth of research focusing on the application of Multivariate Analysis (MVA) tools and miniaturized setups for LIBS and Raman data fusion. Such approaches have the potential to enhance the efficiency and portability of spectroscopic analyses, particularly in resource-constrained environments such as space exploration missions (Gaft, M., Nagli, L., and Panczer, G. 2012).

In light of these considerations, this study aims to contribute to the existing body of literature by investigating the fusion of LIBS and Raman spectroscopy data using advanced data analysis tools such as Origin software. By leveraging MVA techniques and compact instrumentation, we seek to expand upon current methodologies and advance the field of data fusion in mineralogical studies and space exploration research.

2.3 Multivariate Data Analysis

Spectroscopic techniques like LIBS and Raman spectroscopy are commonly employed for identifying unknown substances and determining their composition. In the identification process, the entire spectrum is considered to account for all elements (in the case of LIBS) or vibrations (in Raman spectroscopy). Conversely, for quantification purposes, peak intensities are utilized to establish univariate linear regression models, where known concentrations are correlated with the peak area of specific emission lines. However, a drawback of univariate calibration is the failure to consider matrix effects or variations in experimental conditions that affect the entire spectrum, limiting the accuracy of these models. Consequently, multivariate data analysis (MVA) methods, which consider the entire spectrum rather than focusing on individual spectral features, have become standard techniques for both sample identification and quantification in spectroscopic analysis.

Numerous studies have demonstrated the efficacy of MVA methods in identifying and quantifying substances in LIBS data. Today, MVA techniques are widely adopted for the analysis of both LIBS and Raman spectroscopy data. For instance, in the analysis of ChemCam data, major elements are predicted using a combination of partial least-squares regression (PLS-R) and independent component analysis (ICA) (Forni et al., 2013).

In the subsequent sections, two MVA techniques utilized in this thesis will be discussed. Principal component analysis (PCA) was employed for classification purposes, while partial least squares regression (PLS-R) was applied for quantification (Kessler, 2007).

2.3.1 Principal component analysis (PCA)

Principal Component Analysis (PCA) is a method utilized to discern patterns and structures within high-dimensional data by projecting it onto new axes, known as principal components (PCs). This transformation serves to reduce the dimensionality of the data while capturing its essential features. In the PCA process, the new axes are determined successively. For a dataset consisting of n samples, each characterized by m attributes (such as wavelength channels in spectroscopy), the first component points in the direction of the largest variance among the samples in an m-dimensional coordinate system. Mathematically, PCA involves solving an Eigenvalue problem to find these new axes.

$$X = TPT + E \tag{2.4}$$

The original data matrix X is decomposed into the dot product of the score's matrix T and the loading matrix P, along with the residual's matrix E. It is recommended to center the data before performing PCA to ensure that the first component represents more than just the mean of all input samples. The dimensions of T and P are determined by the number of components (k), with each component being a linear combination of the original data. The loadings of individual components in PCA plots represent the correlations of each wavelength channel with that particular component, facilitating the identification of correlations between spectral features in the data. The Unscrambler software was employed for the Multivariate Analyses (MVAs) in this study. For PCA, it utilizes the non-linear iterative partial least squares (NIPALS) algorithm to solve the Eigenvalue problem iteratively, converging after several repetitions of the algorithm (Kessler, 2007).

2.3.2 Partial least squares (PLS) regression

Partial least squares regression (PLS-R) stands out as one of the most commonly utilized multivariate regression techniques. While Principal Component Analysis (PCA) operates in an unsupervised manner, PLS-R is supervised, implying that it integrates prior knowledge about the samples. In spectroscopy, this prior knowledge typically consists of known concentrations of elements or groups in characterized calibration samples. Therefore, PLS-R involves a multivariate regression between the data matrix X and a response matrix Y, where this information is stored (Geladi, P., and Kowalski, B. R. 1986). In practical terms, PCA is conducted separately for both X and Y, and the outer relations of both PCAs are expressed as follows:

$$X = TP^T + E \tag{2.5}$$

$$Y = UQ^T + F \tag{2.6}$$

Here, T and U represent score matrices, P and Q denote loading matrices, and E and F signify residual matrices. In the context of PLS, the components are commonly referred to as latent variables (LVs).

CHAPTER THREE

3. MATERIALS AND METHODS

3.1 Method of Data Collection

In this research paper we examining planetary geochemical minerals, the data gathered from two prominent databases: the NIST database which is a rich repository of standard spectral information for various elements and compounds commonly used in Laser-Induced Breakdown Spectroscopy and the RRUFF database, a well-curated source providing Raman spectra, X-ray diffraction data, and detailed chemistry for an extensive range of mineral species. These databases serve as critical reference points for the spectral analysis of geochemical minerals pertinent to planetary science. The selection of mineral samples for analysis was focuses on those with significant relevance to planetary surfaces such as the Moon, Mars, or various asteroid bodies.

3.1.1 Raman data

Raman spectra of minerals of astronomical analogues on Earth were collected primarily from RRUFF database. Here, one can find Raman and XRD data of numerous minerals including that of meteorites and their respective synthetic data. Some target minerals that may be found beyond Earth, that is, those that can be of any unearthly origin were selected. These minerals targeted involved chalcanthite, calcite, halite, olivine, gypsum, Nontronite and Quartz. Thus, intensity vs. wavenumber (Raman shift) data of these targets was obtained from RRUFF database website.

Screenshots of some of these data were taken as a sample in the following figures.

```
##NAMES=Chalcanthite
##RRUFFID=R050293
##IDEAL CHEMISTRY=Cu^2+^S^6+^O_4_&#183;5H_2_O
##LOCALITY=79 mine, 4th level, Hayden, Gila County, Arizona, USA
##OWNER=RRUFF
##SOURCE=George Godas, John Callahan
##DESCRIPTION=Blue fibrous crust
##STATUS=The identification of this mineral has been confirmed by X-ray diffraction and chemical analysis
##URL=rruff.info/R050293
##MEASURED CHEMISTRY=Cu_1.00_S_1.00_O_4_·5H_2_O
129.7456, 745.5238
131.6741, 741.7949
133.6025, 735.8936
135.5310, 732.1678
137.4595, 733.3480
139.3879, 733.6468
141.3164, 730.4779
143.2449, 723.3304
145.1733, 714.4413
147.1018, 703.4059
149.0303, 690.3610
150.9587, 678.5061
152.8872, 667.7724
154.8157, 658.0654
156.7441, 649.2462
158.6726, 640.8596
160.6011, 633.8266
162.5295, 628.5413
164.4580, 624.8521
```

Figure 3: Raman Data of Chalcanthite R050293 from 79 mine, Arizona. (Source: rruff.info/)

```
##NAMES=Calcite
##RRUFFID=R040070
##IDEAL CHEMISTRY=CaCO_3_
##LOCALITY=Pryor Mountain, Big Horn County, Montana, USA
##OWNER=RRUFF
##SOURCE=University of Arizona Mineral Museum
##DESCRIPTION=Orange scalenohedral crystals
##STATUS=The identification of this mineral has been confirmed by X-ray diffraction and chemical analysis
##URL=rruff.info/R040070
##MEASURED CHEMISTRY=(Ca_0.99_Mg_0.01_)CO_3_
117.9119, 382.2266
119.8403, 494.9488
121.7688, 617.0251
123.6973, 745.0114
125.6257, 881.5561
127.5542, 931.7645
129.4827, 968.2148
131.4111, 1023.074
133.3396, 1088.147
135.2681, 1138.971
137.1965, 1262.275
139.1250, 1364.376
141.0535, 1546.567
142.9819, 1937.290
144.9104, 2602.847
146.8389, 3418.879
148.7673, 4433.732
150.6958, 6048.733
152.6243, 7120.791
```

Figure 4: Raman Data of Calcite R040070 from Pryor mountain 21346 big horn country. (Source: rruff.info/)

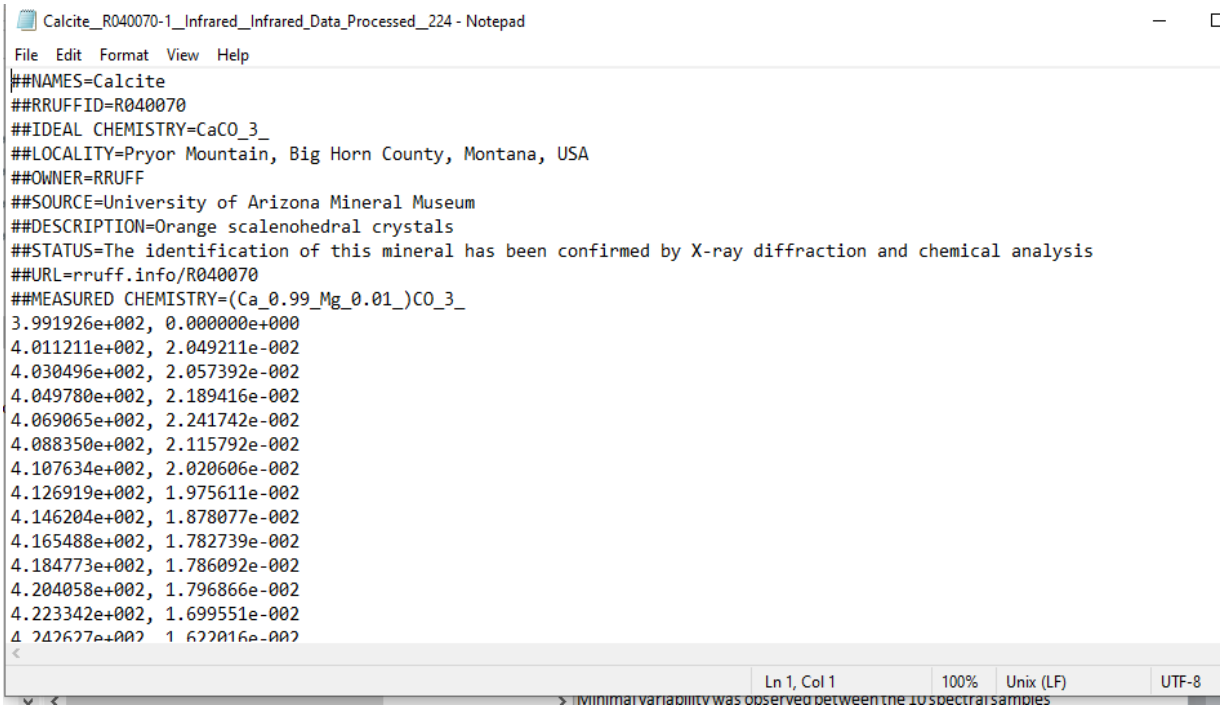

Figure 5: Raman Data of Calcite R040070 from Pryor mountain 224 big horn country montana. (Source: rruff.info/)

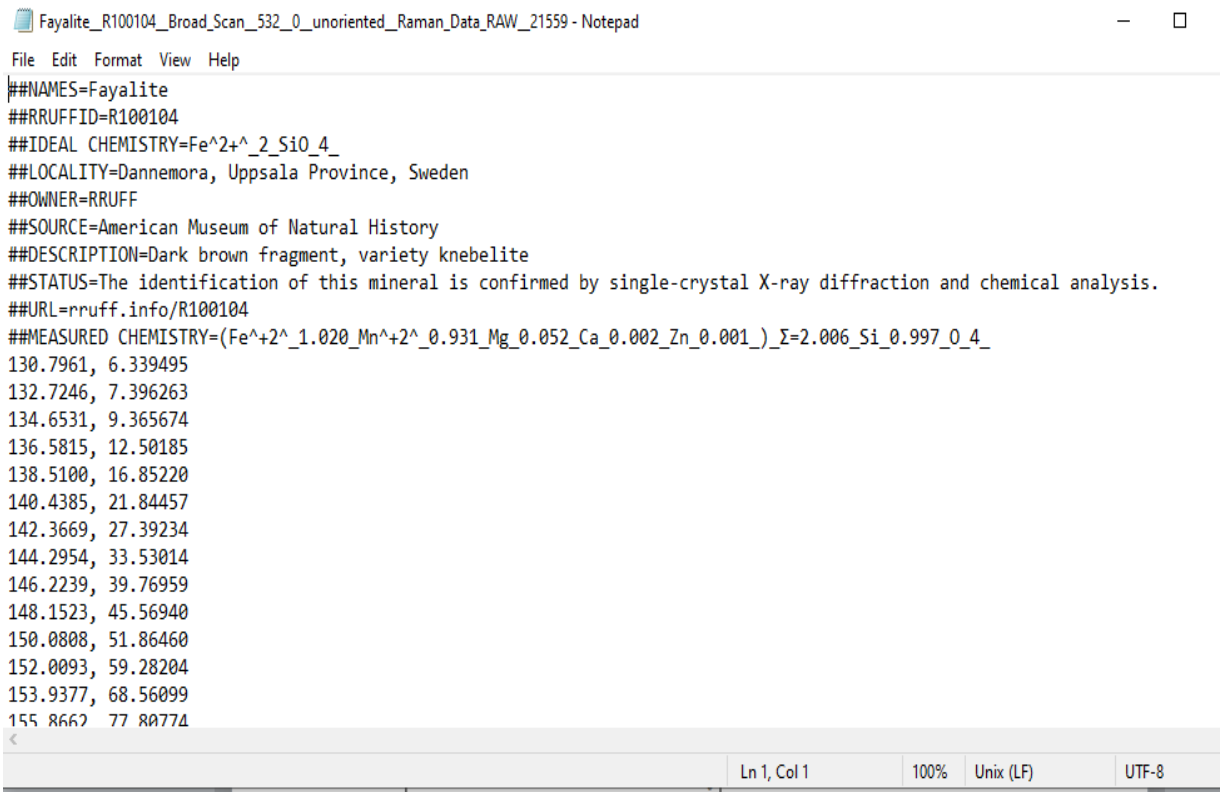

Figure 6: Raman Data of Fayalite R100104 from Dannemora 21559 swede. (Source: rruff.info/)

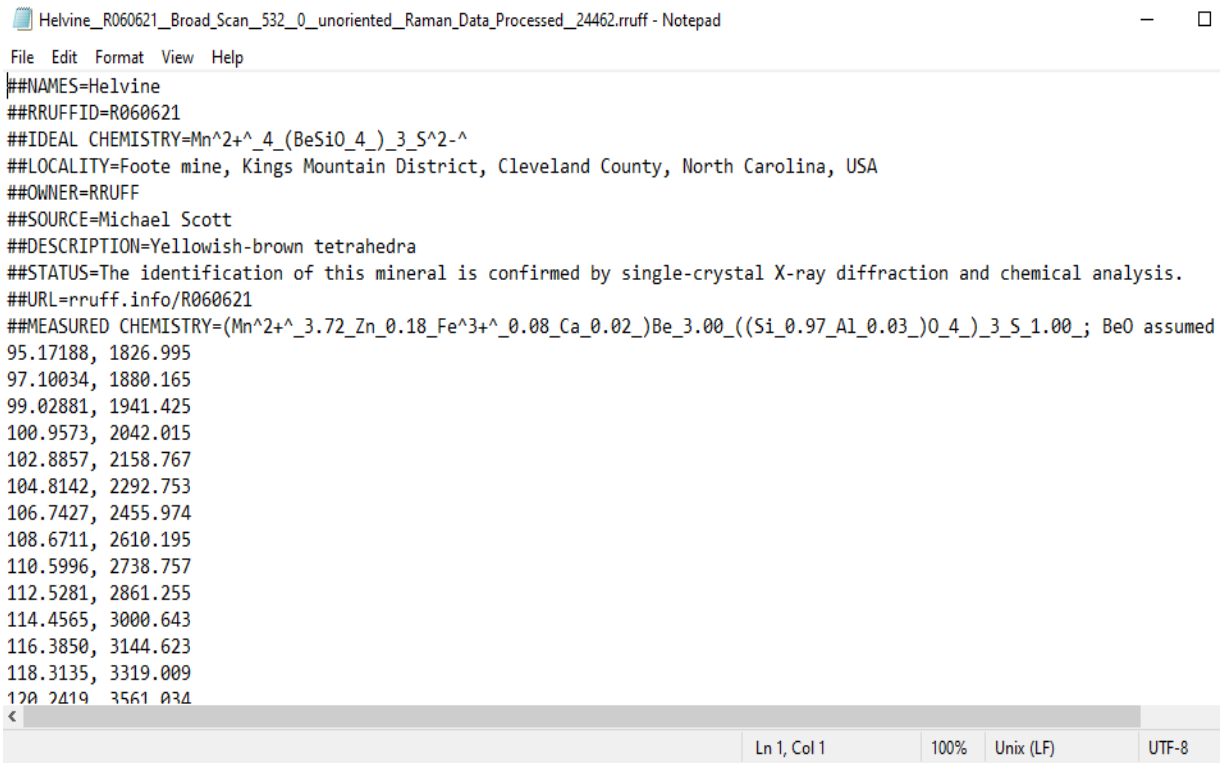

Figure 7: Raman Data of Helvine R060621 from foote mine kings 24462 mountain district. (Source: rruff.info/)

3.1.2 LIBS data

LIBS spectra of minerals of astronomical analogues on Earth were collected from the National Institute of Standards (NIST) LIBS database. The elemental composition of minerals such as Fayalite (Fe_2SiO_4), Chalcanthite ($CuSO_4 \cdot 5H_2O$), Calcite ($CaCO_3$), Forsterite (Mg_2SiO_4), Gypsum ($CaSO_4 \cdot 2H_2O$), Halite (NaCl), Nontronite ($Na_{0.3}Fe^{3+}_2(Si,Al)_4O_{10}(OH)_2 \cdot nH_2O$), and Quartz ($SiO_2$), the NIST (National Institute of Standards and Technology) database used utilized for precise and accurate analysis. The NIST database provides comprehensive information on various elements' X-ray diffraction patterns and spectral data, which can be employed for mineral identification and verification. For each mineral, the elemental analysis involves several steps. First, the chemical formula of the mineral is broken down into its constituent elements. Then, using the NIST database, the atomic weights, standard reference patterns, and characteristic spectral lines of these elements are identified. Thus, intensity vs. wavelength data of these targets was obtained from this website of database.

Screenshots of some of these data were taken as a sample in the following figures.

Cu I-III (new window)

Cu I-III Energy Levels
Cu I-III Line Wavelengths and Classification
Cu I-III Transition Probabilities

Ion	Observed Wavelength Air (nm)	Ritz Wavelength Air (nm)	Rel. Int. (?)	A_{ki} (s^{-1})	Acc.	E_i (cm^{-1})		E_k (cm^{-1})
Cu I	200.1672	200.16723	12a			0.000	–	49 942.051
Cu I	200.1947	200.19472	6a			0.000	–	49 935.195
Cu II	200.29033	200.29020	73000			88 605.096	–	138 516.49
Cu I	200.9252	200.92510	12a			11 202.618	–	60 956.32
Cu II	200.932	200.928239	6800			68 730.8876	–	118 483.8135
Cu II	201.298037	201.298041	1800000	2.5e+08	C	66 418.6849	–	116 080.2237
Cu III	201.322		200					
Cu II	201.55822	201.558222	1400000	2.1e+07	C+	23 998.3718	–	73 595.8143
Cu II	201.58660	201.58649	39000			88 926.002	–	138 516.49
Cu II	201.68964	201.689673	1700000	8.1e+06	C+	21 928.7326	–	71 493.8548
Cu II	201.76096	201.760977	160000			71 531.542	–	121 079.1501
Cu II	202.21913	202.219147	170000	1.14e+07	C+	68 447.7349	–	117 883.0985

Figure 8: LIBS Data of Cu. (Source: rruff.info/)

Query NIST Bibliographic Databases for
O I-III (new window)

O I-III Energy Levels
O I-III Line Wavelengths and Classification
O I-III Transition Probabilities

Ion	Observed Wavelength Air (nm)	Ritz Wavelength Air (nm)	Rel. Int. (?)	A_{ki} (s^{-1})	Acc.	E_i (cm^{-1})		E_k (cm^{-1})
O III	201.327		360					
O II	201.6589	201.65822	10	8.57e+06	C	208 392.258	–	257 965.11
O II	202.0340	202.03299	12	1.99e+07	C	208 484.202	–	257 965.11
O II	202.1445	202.14364	10	1.18e+07	C	208 346.104	–	257 799.93
O II	202.2768	202.2800	10			228 723.84	–	278 144.33?
O II		202.2788				228 723.84	–	278 144.62
O II	202.3332	202.33250	10	3.77e+06	C	208 392.258	–	257 799.93
O II	202.3740	202.3755	12bl			228 747.45	–	278 144.62
O II	202.5694	202.57048	5	4.70e+06	C	208 346.104	–	257 695.74
O I		202.643		2.82e+05	C	88 630.587	–	137 962.5
O I		202.643		1.05e+05	D	88 630.587	–	137 962.5

Figure 9: LIBS Data of O. (Source: rruff.info/)

Query NIST Bibliographic Databases for
Ca I-III (new window)

Ca I-III Energy Levels
Ca I-III Line Wavelengths and Classification
Ca I-III Transition Probabilities

Ion	Observed Wavelength Air (nm)	Ritz Wavelength Air (nm)	Rel. Int. (?)	A_{ki} (s^{-1})	Acc.	E_i (cm^{-1})		E_k (cm^{-1})
Ca III	200.0895	200.08954	1400	2.6e+08	B	278 621.01	–	328 582.45
Ca III	200.1402	200.1404	1100	4.9e+06	C	227 432.11	–	277 380.86
Ca III	200.2987	200.2986	1100	3.0e+08	B	281 139.55	–	331 048.86
Ca III	201.4103	201.4104	1000	3.2e+06	C	227 388.56	–	277 022.40
Ca III	201.8697	201.86956	1300	3.5e+08	B	281 882.24	–	331 403.20
Ca III	202.0772	202.07762	1000			278 621.01	–	328 090.99
Ca III	202.6050	202.60553	1000	2.16e+08	B	278 621.01	–	327 962.11
Ca III	202.6589	202.65914	470	3.6e+07	C	282 075.15	–	331 403.20
Ca III	202.7667	202.76681	470	9.9e+06	C	278 621.01	–	327 922.87
Ca III	203.3358	203.3358	1700	1.51e+08	B	277 022.40	–	326 186.32
Ca III	204.1538	204.1540	1700	2.6e+07	C	228 413.95	–	277 380.86

Figure 10: LIBS Data of Ca. (Source: rruff.info/)

Query NIST Bibliographic Databases for
Si I-III (new window)

Si I-III Energy Levels
Si I-III Line Wavelengths and Classification
Si I-III Transition Probabilities

Ion	Observed Wavelength Air (nm)	Ritz Wavelength Air (nm)	Rel. Int. (?)	A_{ki} (s^{-1})	Acc.	E_i (cm^{-1})		E_k (cm^{-1})
Si III		200.1072		1.91e+07	D	199 164.10	–	249 121.14
Si II		200.416		4.76e+06	D	76 665.35	–	126 545.4
Si II		200.495		4.75e+06	D	76 665.35	–	126 525.8
Si III		200.914		3.60e+07	D+	204 828.06	–	254 584.6
Si III		200.9899		2.61e+07	D	205 029.09	–	254 766.75
Si I	201.097		30					
Si II		201.492		3.31e+07	D+	76 665.35	–	126 279.0
Si II		201.666		3.39e+07	C	76 665.35	–	126 236.4
Si III		204.9903		2.49e+07	D+	165 765.00	–	214 532.17
Si I	205.483		50					

Figure 11: LIBS Data of Si. (Source: rruff.info/)

3.2 Method of Data Analysis

The first step of data analysis consisted of the selection of key spectral indicators for both Raman and LIBS datasets. To do so, the LIBS and Raman spectra data collected from the sample mixtures described in Section 3.1 were first pre-processed (baseline correction and intensity normalization) using the Origine software. i.e., each element is associated with a specific wavelength (for LIBS) or mineral phases are linked to a potentially specific wavenumber (for Raman). Afterwards, the same software was used to evaluate the correlation between the dependence of characteristic spectral features (peak position, intensity, etc.) with the concentration ratio between sample mixtures.

When we electrolyte minerals with lasers using a technique called Laser-Induced Breakdown Spectroscopy, we get spectra, which are like the mineral's fingerprints. In our study, we took a close look at seven different mineral samples and checked their fingerprints. We did this a number of times for each mineral and mixed the results together, then merged for detailed analysis.

3.2.1 Raman Spectral Analysis

The Raman spectral analysis of minerals imported the spectral data into Origin software. The imported data were processed to identify and analyze the characteristic peaks. Using Origin, a graph was plotted that clearly illustrated the prominent Raman shifts corresponding to the vibrational modes of the minerals structure. i.e. Calcite, a carbonate mineral, exhibits prominent Raman peaks that correspond to the symmetric stretching and bending modes of the carbonate ion ($CO3^{2-}$). These spectral characteristics, verified using the National Institute of Standards and Technology (NIST) database, confirm the mineralogical identity of calcite and provide insights into its molecular structure. Raw spectral data is imported into the software from an external source or entered manually. The software processes the data, which may include baseline correction and normalization. The processed data is then plotted as a spectrum, showing peaks that correspond to different molecular vibrations. It’s analyzing the spectrum to identify substances or molecular structures based on the characteristic absorption peaks.

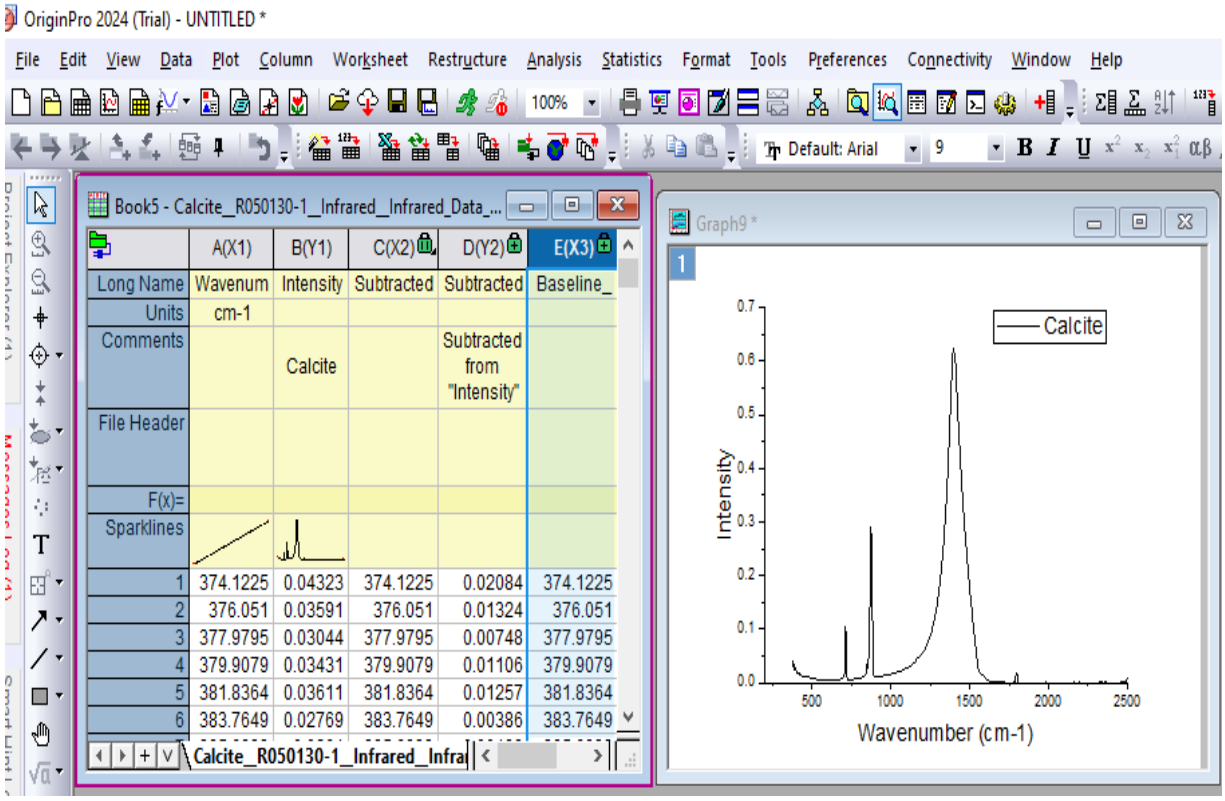

Figure 12: Graphical illustration for Raman spectra of calcite Origin.

3.2.2 LIBS Spectral Analysis

The LIBS spectral analysis of Calcite ($CaCO_3$) imported the spectral data into Origin software. The imported data were processed to identify and analyze the characteristic peaks of calcite. Using Origin, a graph was plotted The LIBS spectra of two calcium-based minerals, i.e. calcium carbonate (Calcite, CaCO3) and calcium sulfate dihydrate (gypsum, CaSO4.2H2O). In both cases, all the major emission lines of calcium were observed throughout the spectral region. The LIBS spectra of calcite, gypsum and calcium sulfate appear very similar, as expected since the major cations present in all these samples are calcium (Ca). On the basis of LIBS alone, these samples cannot thus be distinguished from each other. However, a weak Hydrogen emission line observed at 656.28 nm for the gypsum sample, indicates that it may be a hydrated sample, namely, Gypsum.

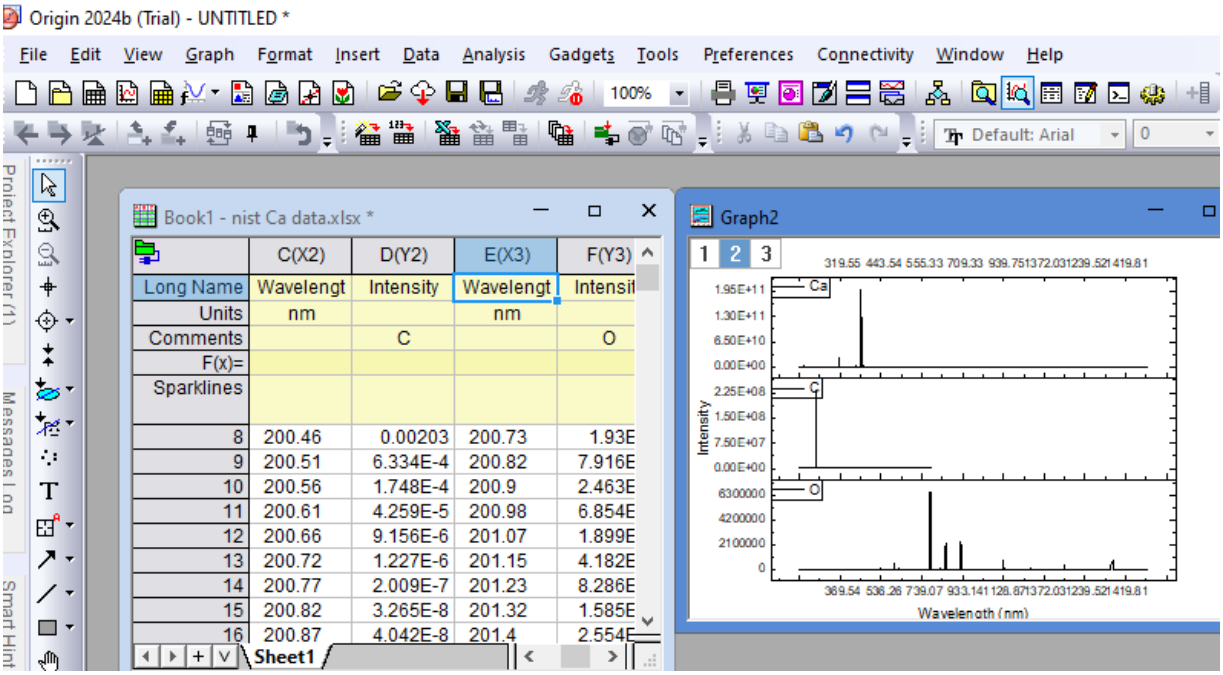

Figure 13: Graphical illustration for LIBS Data Origin.

The LIBS spectra for fayalite, were recorded over the wavelength range of 200-1500 nm. The spectra revealed that fayalite primarily consists of iron (Fe), silicon (Si), and oxygen (O), with iron being the dominant element detected. However, the olivine-based minerals such as fayalite and forsterite based solely on LIBS data.

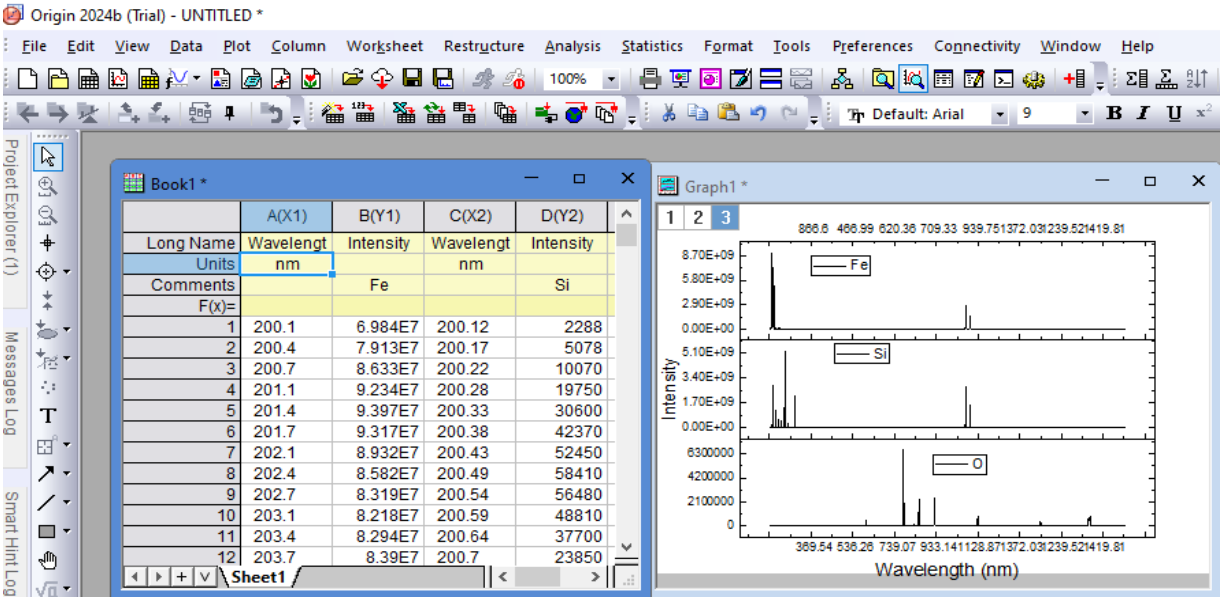

Figure 14: Graphical illustration for LIBS Data Origin.

CHAPTER FOUR

4. RESULTS AND DISCUSSION

4.1 Results

4.1.1 Raman spectra molecular identification

Fayalite (Fe_2SiO_4)

Here, Raman spectra of four Fayalite minerals were presented from different four origins; R100104 the Dannemora Uppsala Province, R100103 Franklin Sussex County, X050077 synthetic and X050076.4. Each of these samples likely has its own unique Raman spectrum, which show peaks corresponding to the vibrational modes of the mineral's molecular structure. The spectra of different samples, the positions and intensities of these peaks vary depending on factors such as crystallographic orientation, impurities, and structural defects. A peak representing a specific vibrational mode appeared at slightly different wavenumbers (frequency units in Raman spectroscopy) or have different intensities in spectra from different samples.

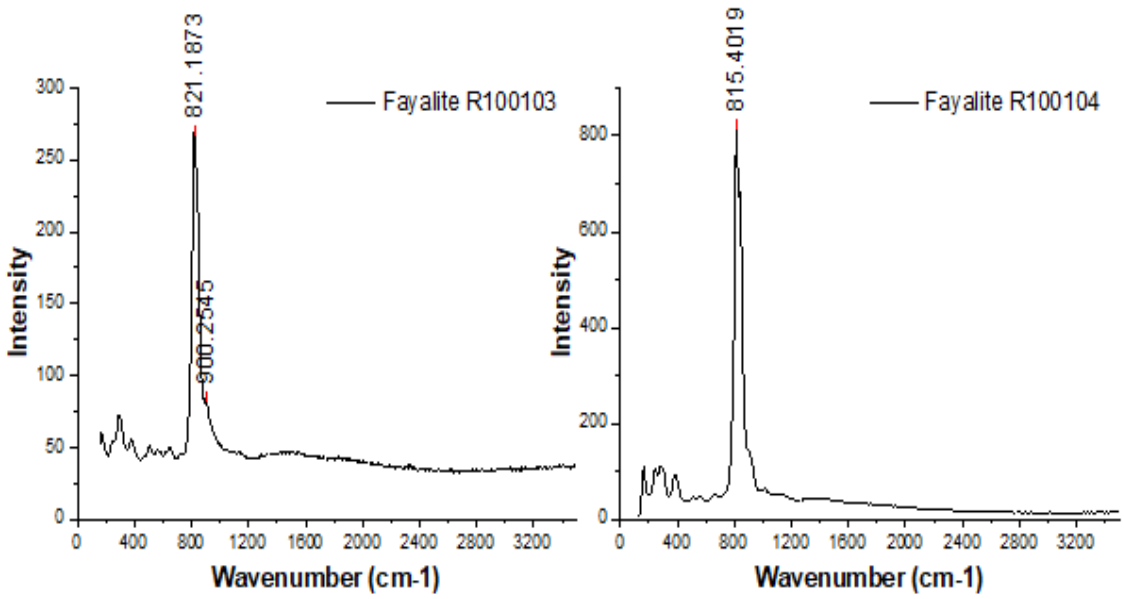

Figure 15: Results on the Raman spectra datasets of Fayalite for R100103 and R100104.

The above figure shows two Raman spectra for Fayalite, labeled R100103 and R100104. In the spectrum of Fayalite R100103, there is a prominent peak at 821.1873 cm^{-1}. For Fayalite R100104, the most intense peak appears at 815.4019 cm^{-1}. Both spectra exhibit a major peak around 820 cm^{-1}, indicating similar structural characteristics in the samples, with Fayalite R100103 showing a peak at 821.1873 cm^{-1} and Fayalite R100104 at 815.4019 cm^{-1}. This suggests slight differences in their vibrational modes. Additionally, the peak at 500.2545 cm^{-1} in the Fayalite R100103 spectrum, absent in the Fayalite R100104 spectrum, points to a difference in the vibrational modes between the two samples.

The intensity of the major peak in Fayalite R100104 is significantly higher than that in Fayalite R100103, which could imply a higher concentration of the phase or differences in crystal quality or orientation. Both spectra display characteristic Raman signatures for Fayalite, yet the differences in peak positions and intensities suggest slight variations in crystal structure or composition. Overall, while both samples exhibit similar vibrational characteristics, the variations in the spectra indicate differences in their structural properties.

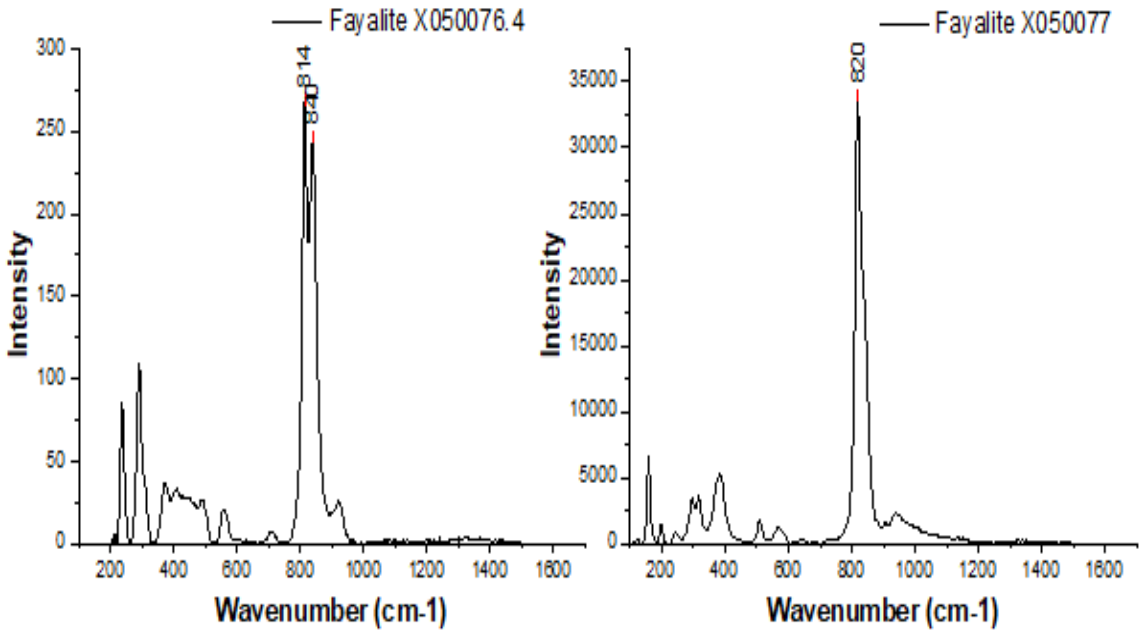

Figure 16: Results on the Raman spectra datasets of Fayalite for X050076.4 and X050077.

The above figure shows the spectroscopic analysis of Fayalite with two distinct samples labeled "Fayalite X050706.4" and "Fayalite X050707." The left graph shows a prominent peak at approximately 350 cm^{-1} and several smaller peaks between 200 and 600 cm^{-1}, suggesting characteristic vibrational modes of the mineral's molecular structure. The right graph features a significant peak at around 820 cm^{-1}, with additional minor peaks spread at 110 cm^{-1}. Both graphs exhibit baseline intensity near zero, except at the peaks, indicating the specific interactions of Fayalite with light within this spectral region. These results are crucial for material science research and quality control processes involving Fayalite, providing insights into its composition at a molecular level. The sharpness and height of the peaks are indicative of the purity and concentration of Fayalite in the samples analyzed.

Forsterite

Here, Raman spectra of four Forsterite minerals were presented from different four origins; R050117 Sapat Gilgit, R060539 Sri Lanka, X050081 East Africa and X050080.4 Synthetic end member. By comparing the Raman spectra of Forsterite samples from different origins, variations in peak positions, intensities, and spectral features was identifyed. These differences arises from crystal structure, geological setting, and post-depositional processes.

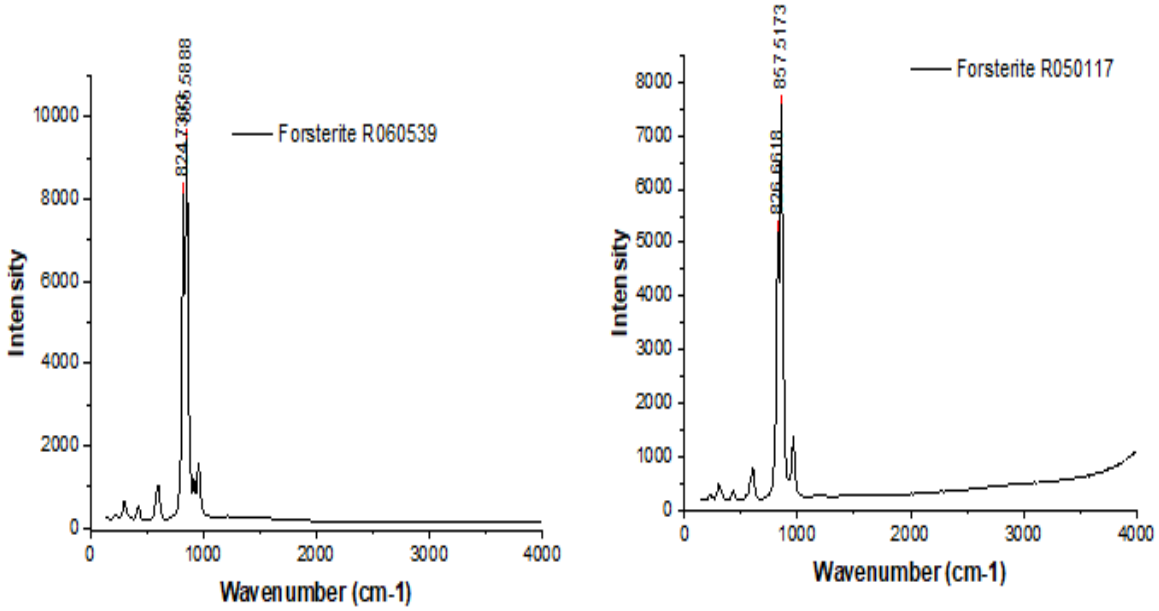

Figure 17: Results on the Raman spectra datasets of Forsterite for R060539 and R050117.

The image presents two graphs that analyze the intensity of Forsterite samples labeled "Forsterite R060539" and "Forsterite ROS0117." Both graphs plot intensity against wavenumber, with the most notable peak occurring just before 1000 cm^{-1}. The left graph shows a higher intensity peak compared to the right, indicating a stronger presence or concentration of Forsterite in sample R060539. These graphs are essential for comparing the characteristics of Forsterite samples, particularly in mineralogy and materials science, where understanding mineral compositions is crucial. The data suggests that both samples contain Forsterite, but with varying intensities, which could be due to differences in sample purity, size, or preparation methods. The spectroscopic analysis provides a non-destructive way to study the samples' molecular structure and composition.

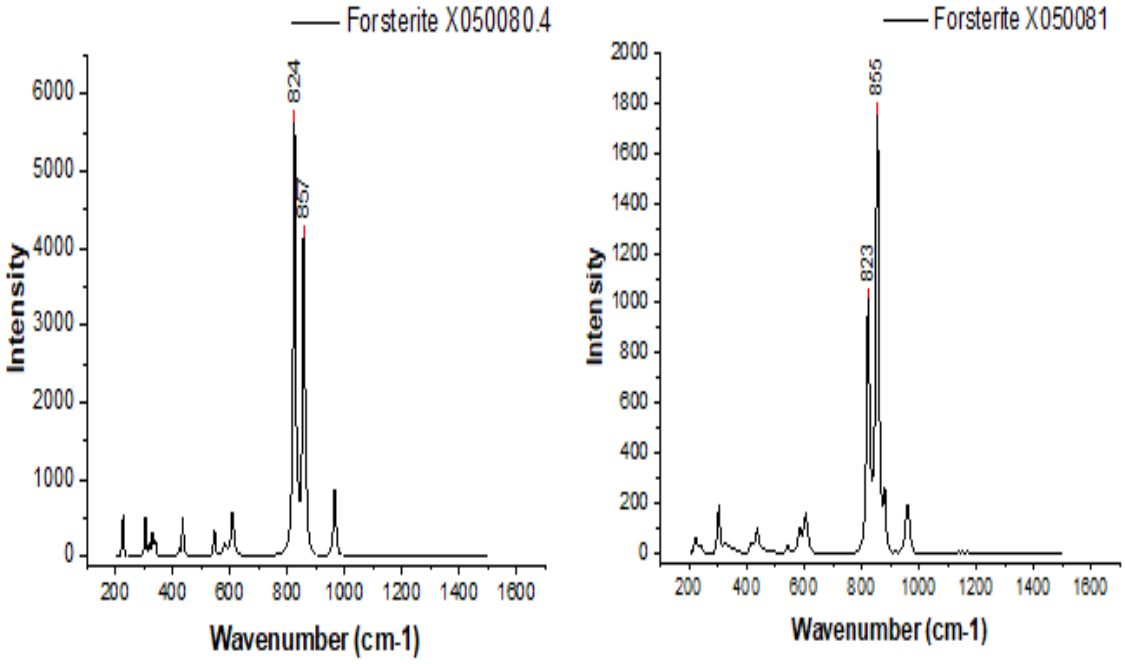

Figure 18: Results on the Raman spectra datasets of Forsterite for X050080.4 and X050081.

The image features two graphs that represent the spectroscopic analysis of Forsterite samples, labeled "Forsterite X05008.04" and "Forsterite X05081." The left graph shows a significant peak at approximately 824 cm^{-1} with intensity just above 6000, along with other smaller peaks, particularly around 400 and 1000 cm^{-1}. The right graph displays a similar pattern, with the most substantial peak at roughly 835 cm^{-1} and intensity close to 1600. These peaks are indicative of

the molecular structure and composition of Forsterite, and the differences in peak intensities and wavenumber shifts suggest variations between the two samples.

Gypsum

Here, Raman spectra of two **Gypsum** minerals were presented from different two origins; R040029.1 Twin Buttes Pima County and X0500098 Lake Mead Arizona.

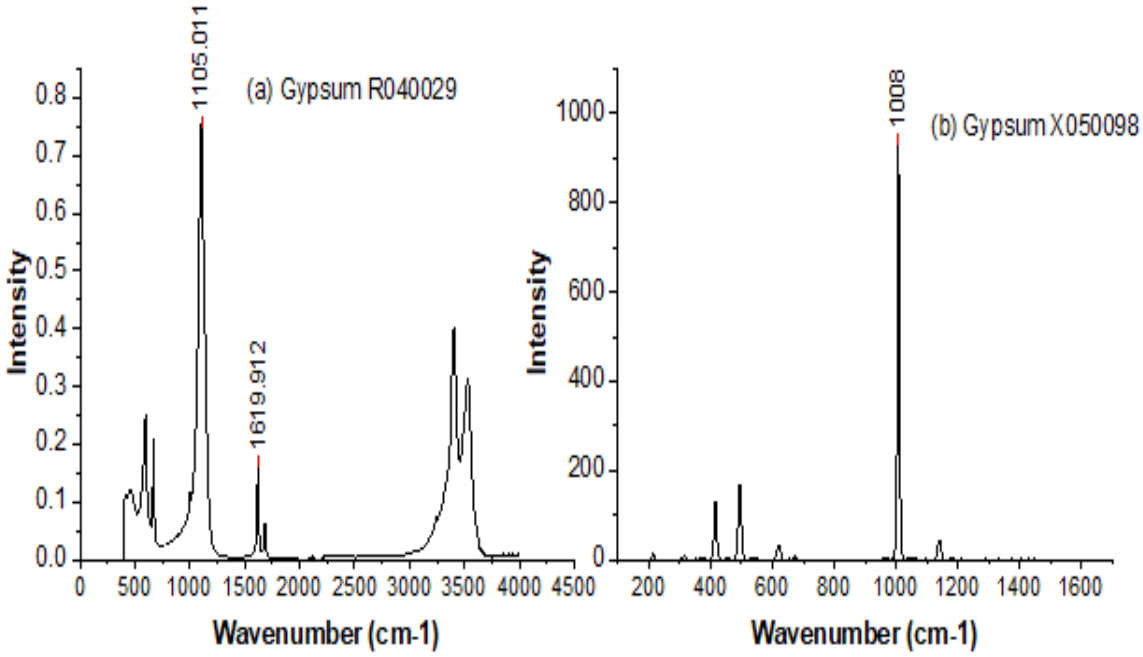

Figure 19: Results on the Raman spectra datasets of Gypsum Origin

The image showcases two graphs that analyze the intensity of peaks across different wavenumbers for Gypsum samples. The left graph, labeled "Gypsum R040029," features multiple peaks, with the most significant at approximately 1015 cm^{-1} and smaller peaks around 1620 cm^{-1} and 3400 cm^{-1}. The right graph, labeled "Gypsum X050098," presents a single dominant peak at roughly 1008 cm^{-1}. These graphs, likely from infrared spectroscopy, are used to identify and compare gypsum samples based on their absorption bands, which is vital for scientific research or quality control in material identification. The data indicates that while both samples contain gypsum, the left sample has a more complex spectrum, suggesting additional components or variations in purity. The right sample's spectrum is simpler, with a single

pronounced peak, implying a more uniform composition. This analysis is crucial for understanding the molecular structure and characteristics of gypsum.

Nontronite

Here, Raman spectra of two **Nontronite** minerals were presented from different two origins; X050120 Twin Buttes Pima County and X050121 Lake Mead Arizona. Both graphs show a series of sharp peaks, which are indicative of the vibrational modes of the molecules in the Nontronite samples.

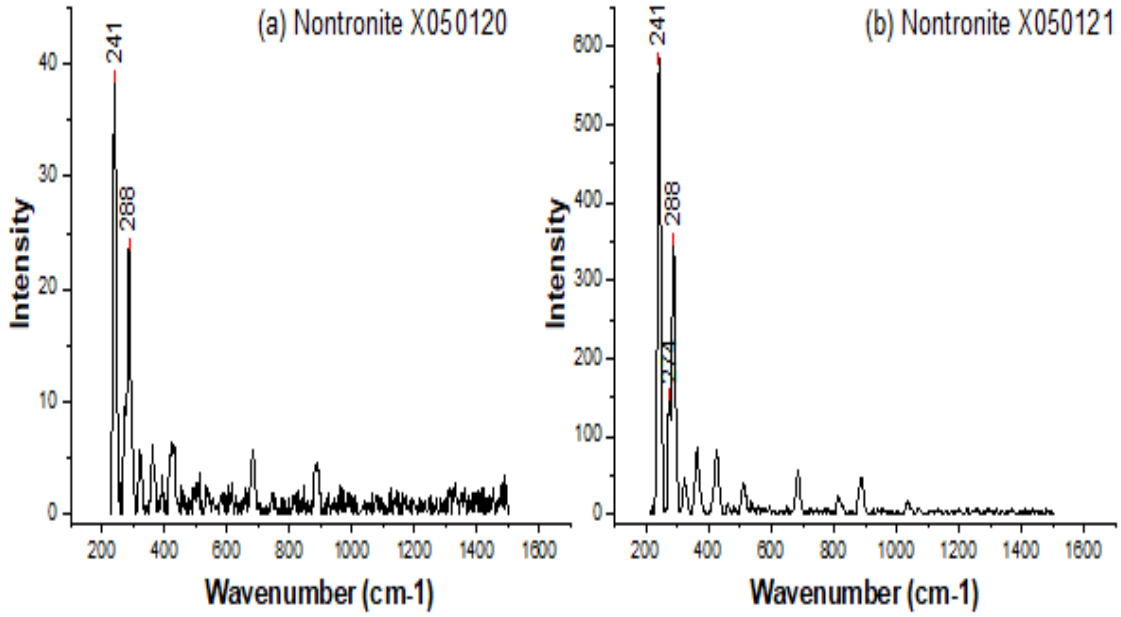

Figure 20: Results on the Raman spectra datasets of Nontronite Origin

The image contains two graphs that illustrate the spectroscopic analysis of Nontronite samples, labeled as (a) Nontronite XOS0120 and (b) Nontronite XOS0121. Both graphs show a prominent peak at approximately 288 cm^{-1}, which is a characteristic feature of Nontronite's molecular structure. The intensity scale differs between the two graphs, with graph (a) ranging up to 2.4 and graph (b) up to 800, suggesting different concentrations or sample conditions. These peaks are significant as they provide insights into the physical properties of the samples, such as their composition and purity. The rest of the spectra display smaller peaks and troughs, which may represent other molecular interactions within the samples. This type of data is

essential for material scientists and researchers who analyze minerals and need to understand their unique spectral signatures. The red text highlighting the peak at 288 cm^{-1} draws attention to this important feature in both samples.

Quartz

Here, Raman spectra of three **Quartz** minerals were presented from different three origins; R040031 Spruce Claim King County, R050125 Linopolis, Minas Gerais and R110108 synthetic. The image displays three graphs, each representing the spectral analysis of Quartz samples. The top left graph, labeled "Quartz R110108," and the top right graph, "Quartz R040031," both show a prominent peak at approximately 465 cm^{-1}, which is characteristic of the Quartz mineral. The bottom left graph, "Quartz R050125," and the bottom right unlabeled graph, follow a similar pattern with the same notable peak. The intensity of this peak varies across the graphs, suggesting differences in the Quartz samples composition or concentration. These spectral fingerprints are crucial for identifying and comparing Quartz samples in scientific research, as they provide insights into the samples molecular structure and interactions with light. The data indicates that while all samples contain Quartz, there may be variations in purity or other mineral inclusions within the samples.

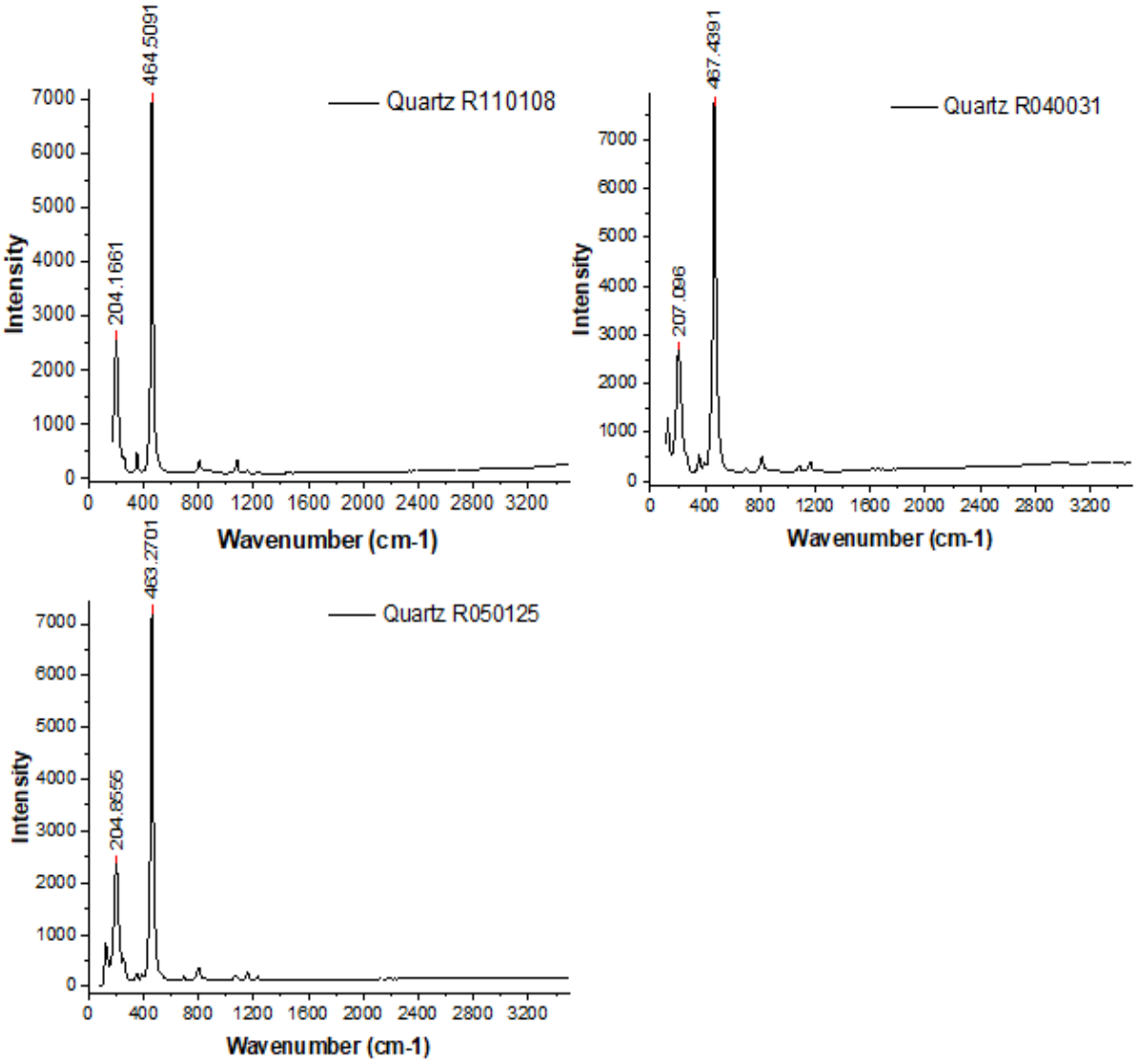

Figure 21: Results on the Raman spectra datasets of Quartz Origin

All graphs show a **similar pattern** of peaks, indicating that the samples are indeed quartz. But there are slight variations in peak **intensity and position**, suggesting differences in sample purity or structure. The consistent presence of characteristic absorption peaks across all samples confirms their quartz composition. The variations in peak details provide insights into the samples' unique properties or quality. The sharp peak at ~465 cm^-1 is a signature feature of quartz and is attributed to the symmetric stretching vibration of the Si-O bond in the quartz crystal lattice. A less intense peak at ~800 cm^-1 is also observed, which is likely due to the bending vibrations of the oxygen atoms in the SiO2 structure. All three graphs show that the molecular structure of quartz is consistent across different samples.

Calcite

Here, Raman spectra of three Calcite minerals were presented from different origins; R040170 from University of Arizona Mineral Museum, R050130 from Dave Bunk Minerals. Additionally, a comparison to Quartz (R050128) is included to provide a broader context for the spectral analysis. These spectra are instrumental in studying the vibrational modes of minerals, which can reveal insights into their structural properties and potential geological origins.

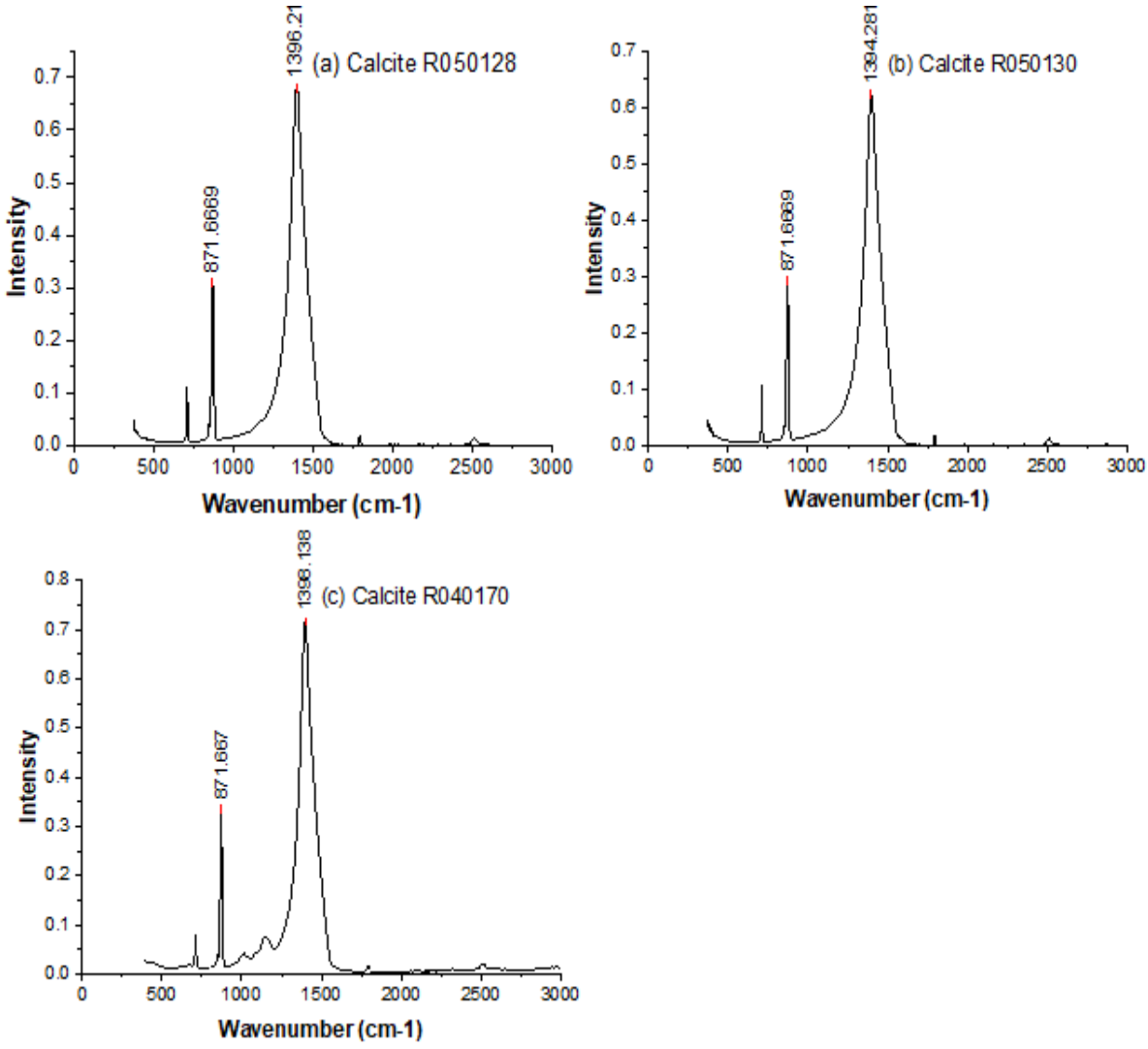

Figure 22: Results on the Raman spectra datasets of Calcite Origin

Each graph plots intensity against wavenumber, with prominent peaks near 700 cm^{-1} and 1400-1500 cm^{-1}, characteristic of carbonate ion vibrations in calcite's structure. These peaks provide insights into the samples' purity and composition, valuable for identifying minerals and

understanding their properties in geology, materials science, and chemistry. The graphs are labeled (a) Calcite R050128, (b) Calcite R050130 and (c) Calcite R040170 each showing variations in peak intensity and position, indicating differences in the physical properties of the calcite samples. Such analysis is crucial for scientific research and quality control processes.

Chalcanthite ($CuSO_4 \cdot 5H_2O$)

Here, Raman spectra of two **Chalcanthite** minerals were presented from different two origins; R520293 79 mine 4th level Hayden and R060102 synthetic.

Graph (a) Chalcanthite R050293: The figure 19 (a) shows the Raman spectrum for a sample labeled "R050293". The **peaks** in the graph correspond to different vibrational modes of the molecules in the sample. The most prominent peak is just before 1000 cm^-1, which could be indicative of a specific molecular bond or structure within the Chalcanthite. **Graph (b) Chalcanthite R060102**: This is also similar to graph (a) but for a different sample labeled "R060102". It shares a similar pattern of peaks with graph (a), suggesting that the two samples are of the same or similar substances. The intensity scale and wavenumber range are the same as in graph (a), allowing for direct comparison between the two.

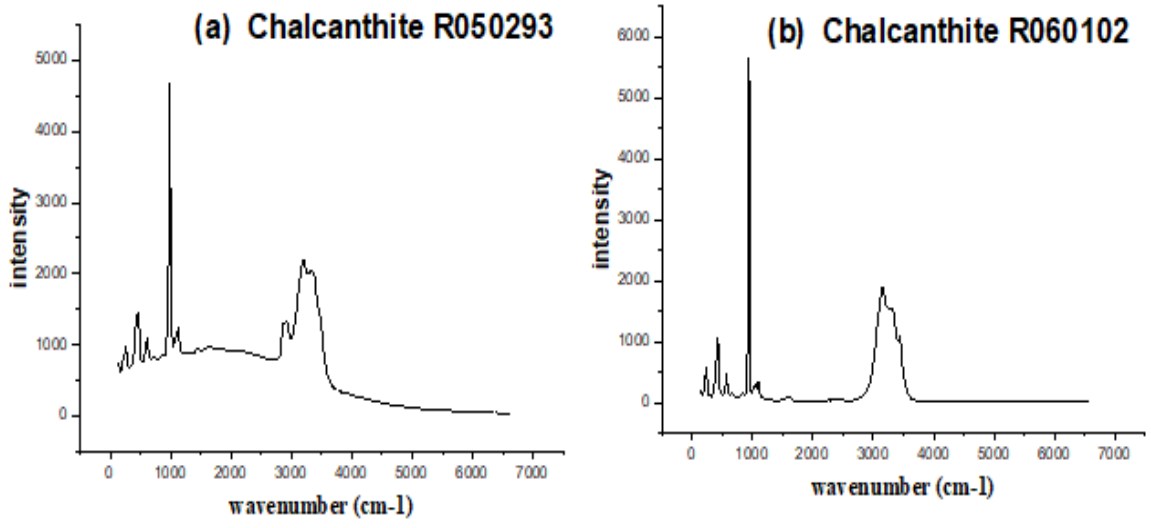

Figure 23: Results on the Raman spectra datasets of Chalcanthite.

Both graphs show a series of peaks, each representing a different vibrational mode of the Chalcanthite molecules. The similarity in the pattern of peaks between the two graphs suggests

that the samples have similar molecular structures. The intensity of the peaks can provide information about the concentration of different molecular bonds or groups within the samples. Therefore, these figures provide a visual representation of the vibrational modes of Chalcanthite, which can be used to deduce its molecular structure and composition.

4.1.2 LIBS spectra for elemental identification

Calsite

Here, elemental Composition of the two LIBS spectra for a Calcite mineral sample, focusing on the elements Calcium (Ca) Carbon (C) and Oxygen (O). The Calcium Spectrum Wavelengths Prominent peaks at approximately 393.366 nm, 396.847 nm, and 422.673 nm. The peaks reach an intensity of up to 2x10^-8 in arbitrary units. The Carbon Spectrum Wavelengths significant peak is observed at approximately 247.857 nm. Similar to calcium, the peak intensity is up to 2x10^-8 in arbitrary units.

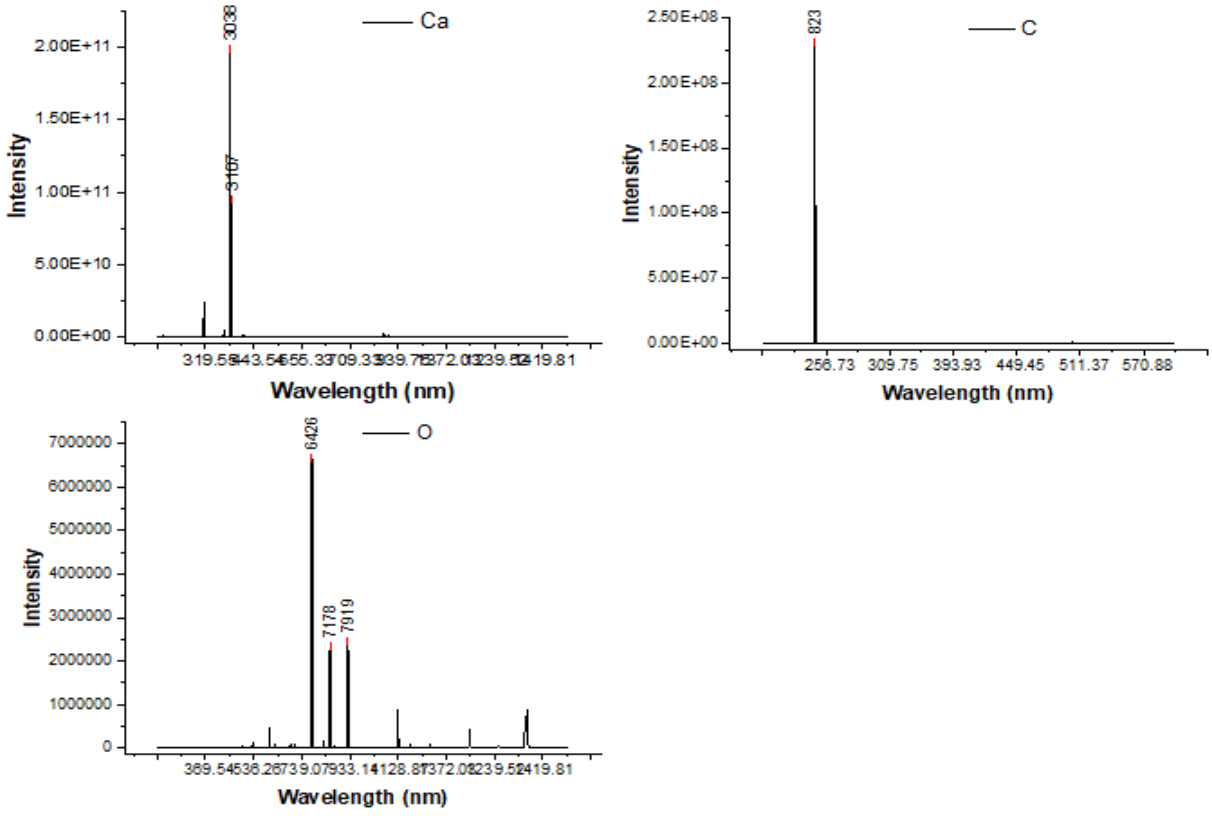

Figure 24: Results for major elements extracted from Libs spectra datasets of Calcite Origin.

Both spectra are plotted with intensity on the y-axis and wavelength on the x-axis. These spectral signatures are crucial for identifying the presence of these elements in the mineral using LIBS technique. The specific wavelengths correspond to the atomic transitions of electrons in calcium and carbon atoms when they return to lower energy states after being excited by the laser pulse. This information is valuable for geochemical analysis and understanding the composition of planetary materials.

Forsterite

The figure presents three spectroscopic graphs, each illustrating the light absorption or emission characteristics of forsterite, a naturally occurring mineral. The top left graph spans wavelengths from 3900 nm to 4000 nm, showcasing sharp peaks, particularly at approximately 3989.23 nm and 3997.53 nm. The top right graph, labeled “Si,” ranges from 30 nm to 40 nm, with distinct peaks near 33.06 nm and a cluster around 36.08 nm, highlighting silicon’s spectral lines in forsterite. The bottom graph extends from about 365.5 nm to 385 nm, with numerous peaks, notably around 369.73 nm and between 373 and 375 nm. These spectra are valuable in mineralogical studies as they reveal the elemental composition and structural properties of forsterite by indicating which wavelengths of light its atoms absorb or emit.

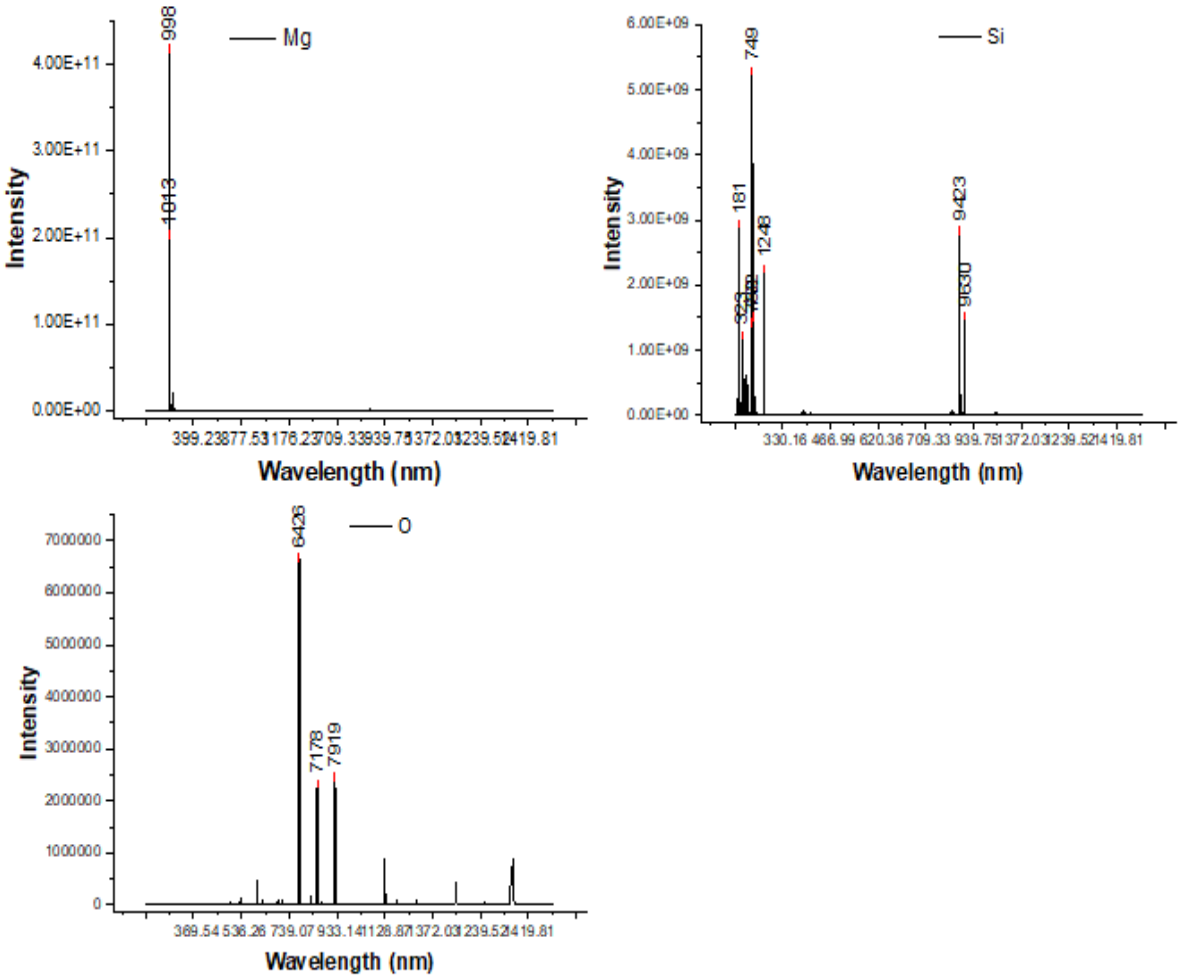

Figure 25: Results for major elements extracted from Libs spectra datasets of Forsterite Origin.

Quartz

The figure shows two graphs related to the spectroscopic analysis of Quartz, focusing on the elements Silicon (Si) and Oxygen (O). The left graph, labeled 'Si,' displays several peaks with notable ones at wavelengths of approximately 1680 nm, 2880 nm, and 3030 nm. The right graph, labeled 'O,' exhibits significant peaks at roughly 365 nm and 777 nm. These peaks represent points where the intensity of light, measured in arbitrary units, is higher due to the presence of these elements. Such spectral data are critical in identifying the elemental composition of Quartz through spectrometry, as each element has characteristic emission or absorption lines at specific wavelengths. This analysis is vital in material science and geology for determining the mineral composition of samples.

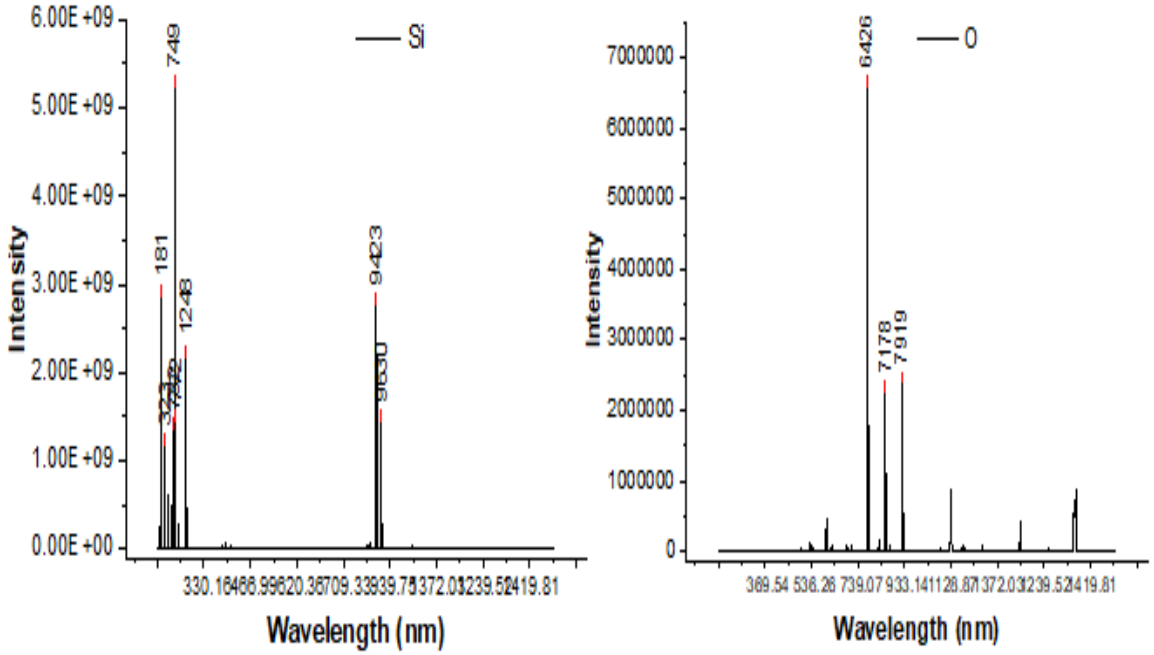

Figure 26: Results for major elements extracted from Libs spectra datasets of Quartz Origin.

Chalcanthite ($CuSO_4 \cdot 5H_2O$)

Here, elemental Composition of the LIBS spectra for chalcanthite showed emission lines for copper (Cu) indicating the presence of this element. Additionally, the sulfur (S), hydrogen (H) and oxygen (O) lines were observed. The peaks observed at approximately 324.75 nm and 327.40 nm indicate the presence of copper. Significant peaks around 288.16 nm and 303.90 nm suggest silicon's presence. Notable peaks near 372.00 nm and 373.70 nm confirm oxygen. Strong emissions near 486.13 nm and another peak just before reaching 434 nm are characteristic of hydrogen. These emission spectra confirm the presence of Copper, Silicon, Oxygen, and Hydrogen in the sample. These elements are identified by their distinct spectral lines at specific wavelengths, which match known transitions for each element.

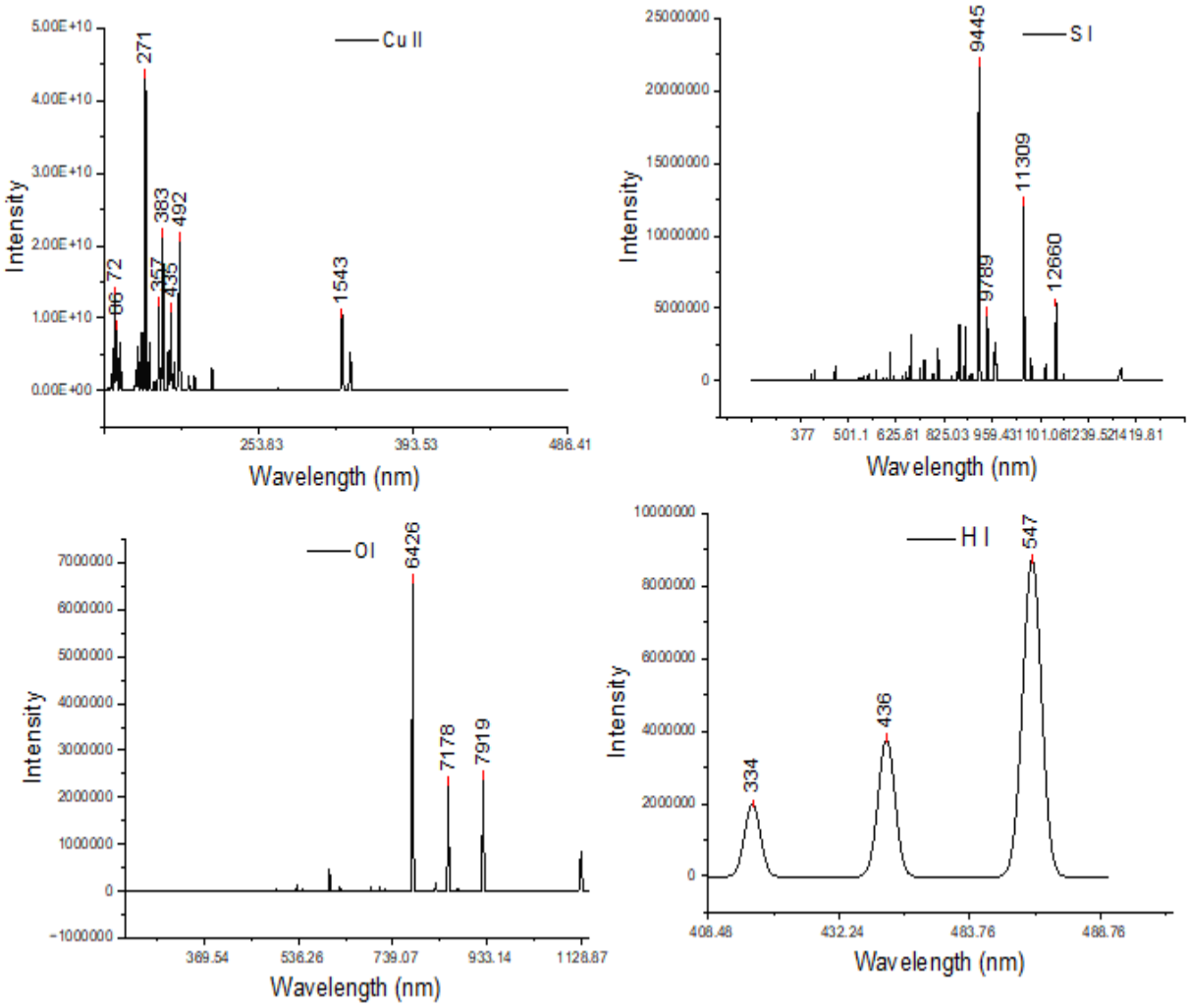

Figure 27: Results for major elements and spectra peaks extracted from LIBS spectra datasets of Chalcanthite.

Fayalite (Fe_2SiO_4)

Here, elemental Composition of the LIBS spectra for **fayalite** indicated the presence of iron (Fe) and silicon (Si), which are the main constituents of the mineral. Strong emission lines for iron were observed at wavelengths such as 452.31 nm and 493.4 nm. These lines are highly intense and undergo self-reversal effects due to the high concentration of Fe in fayalite. Silicon showed prominent lines as well, contributing to the identification of fayalite.

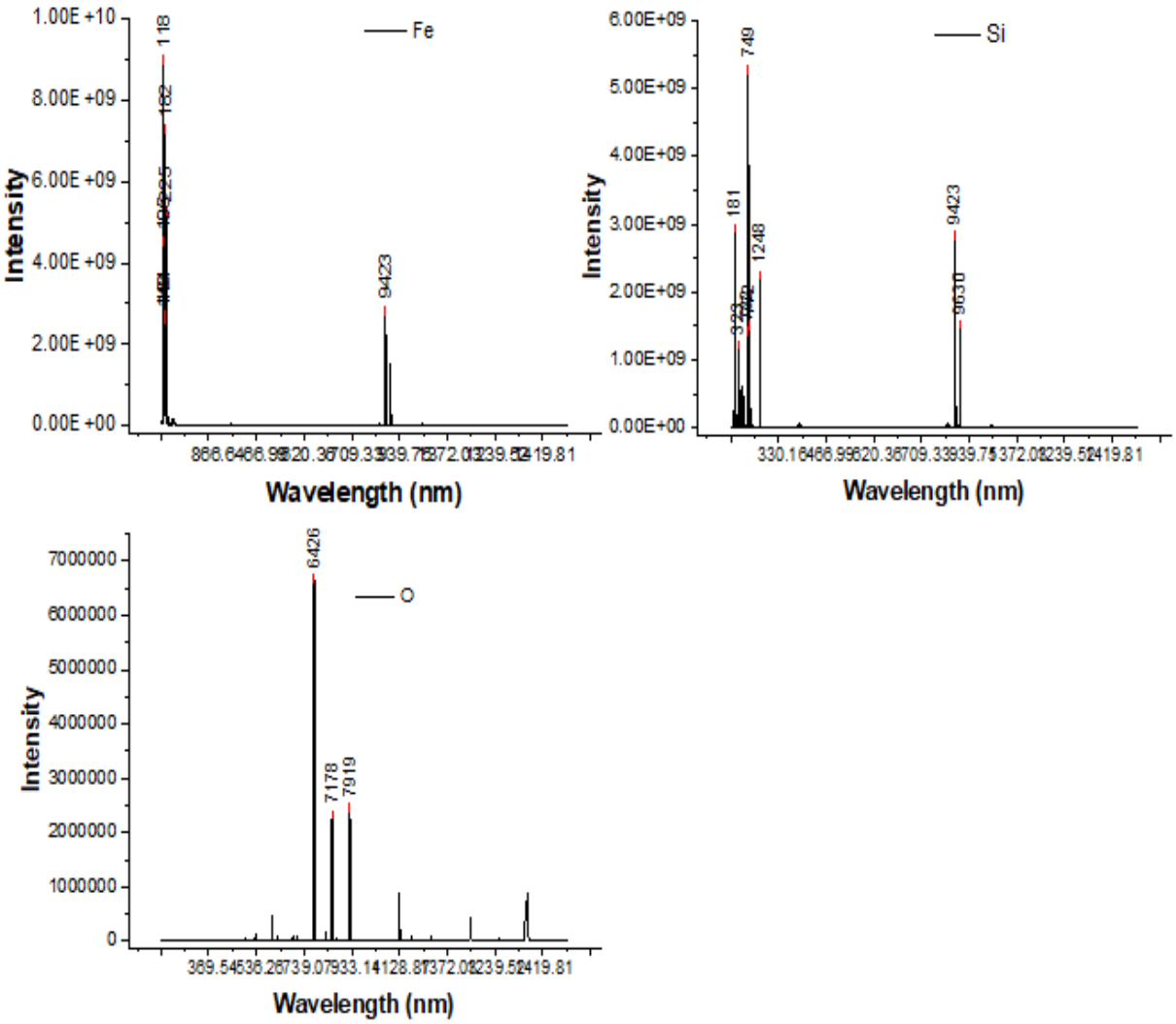

Figure 28: Results for major elements extracted from Libs spectra datasets of Fayalite Origin.

The Figure 28 shows multiple peaks, which are indicative of the wavelengths at which iron emits or absorbs light. The presence of these peaks confirms the presence of iron in the sample. Similar to the iron graph, the silicon graph displays peaks at different wavelengths. These peaks correspond to the spectral lines of silicon, confirming its presence. The oxygen graph also shows peaks, which are characteristic of the oxygen present in the sample.

The graphs provide both qualitative (presence of elements) and quantitative (concentration of elements) information. The intensity of the peaks is proportional to the concentration of the elements in the sample, which is crucial for quantitative analysis.

4.1.3 Combined Analysis of Libs and Raman Spectra

By integrating the LIBS and Raman data in Origin software, we were able to produce comprehensive spectral profiles for the samples. The fusion of LIBS and Raman spectra provided both elemental and molecular information, it enhances our ability to identify and characterize the minerals. For instance, while LIBS effectively detected the presence of iron in fayalite, Raman spectroscopy provided detailed insights into the vibrational modes of the mineral's molecular structure.

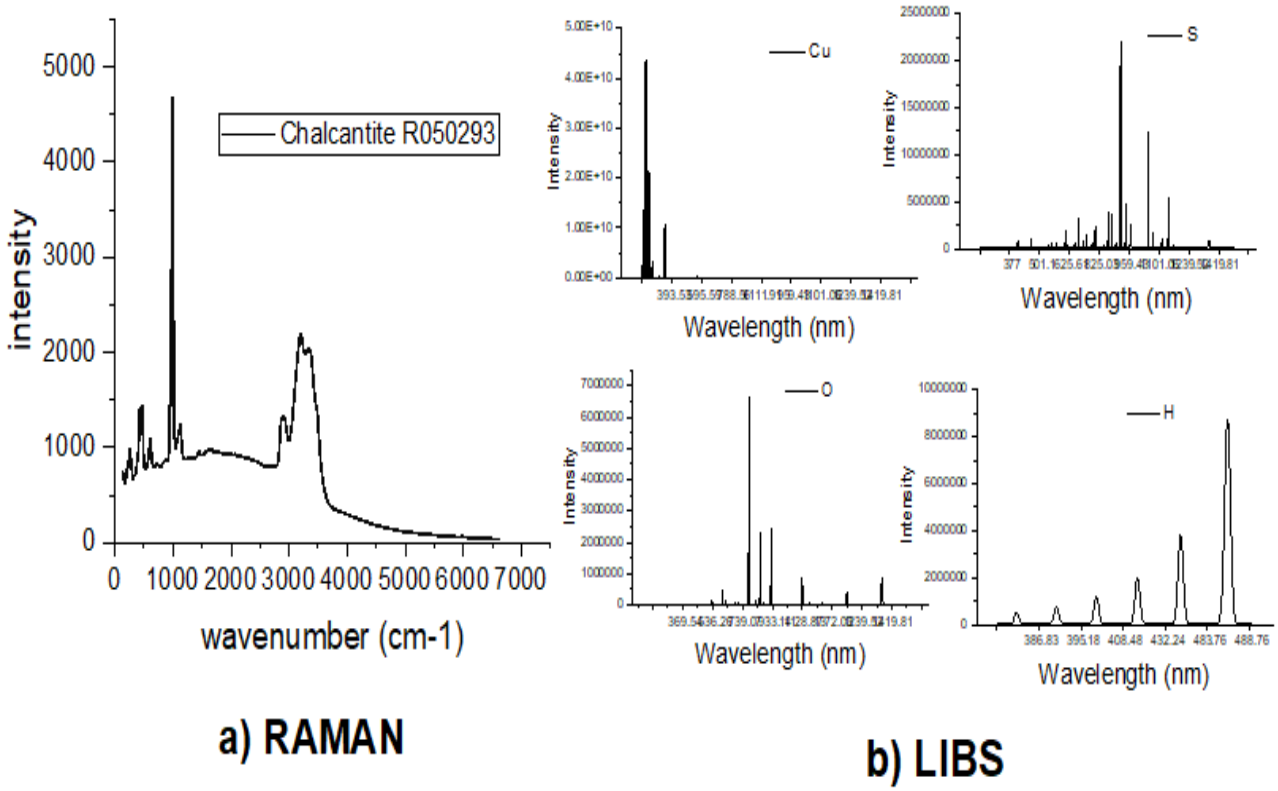

Figure 29: Results on the Raman and LIBS fused datasets of Chalcantite minerals.

The Figure 30 shows fused Raman and LIBS (Laser-Induced Breakdown Spectroscopy) spectra for the mineral Calcite ($CaCO_3$), specifically the sample labeled Calcite R050048. The Raman spectrum is shown on the left, Main Peaks are at 281 cm^{-1}, 714 cm^{-1} and 1087 cm^{-1} The most prominent peak, corresponding to the symmetric stretching mode of the carbonate ion (CO_3^{2-}). The dominant peak at 1087 cm^{-1} is characteristic of the carbonate group in calcite, confirming the presence of calcite. The presence of peaks at lower wavenumbers (281 cm^{-1} and 714 cm^{-1}) related to lattice vibrations indicates a well-crystallized structure. while LIBS Spectra Various

peaks, with the most prominent ones around 393.37 nm and 396.85 nm, indicating the presence of calcium. A significant peak around 247.86 nm, confirming the presence of carbon. Notable peaks around 777.19 nm and 844.63 nm, indicating the presence of oxygen.

Therefore, by fusing the spectra we found the molecular structure and lattice vibrations, confirming the presence of the carbonate ion (CO_3^{2-}) and indicating the crystalline structure of calcite. Also the elemental composition data, confirming the presence of calcium (Ca), carbon (C), and oxygen (O), which are the fundamental elements in calcite. The Raman spectrum's confirmation of calcite through the carbonate ion's vibrational modes is validated by LIBS detecting its constituent elements (Ca, C, and O).

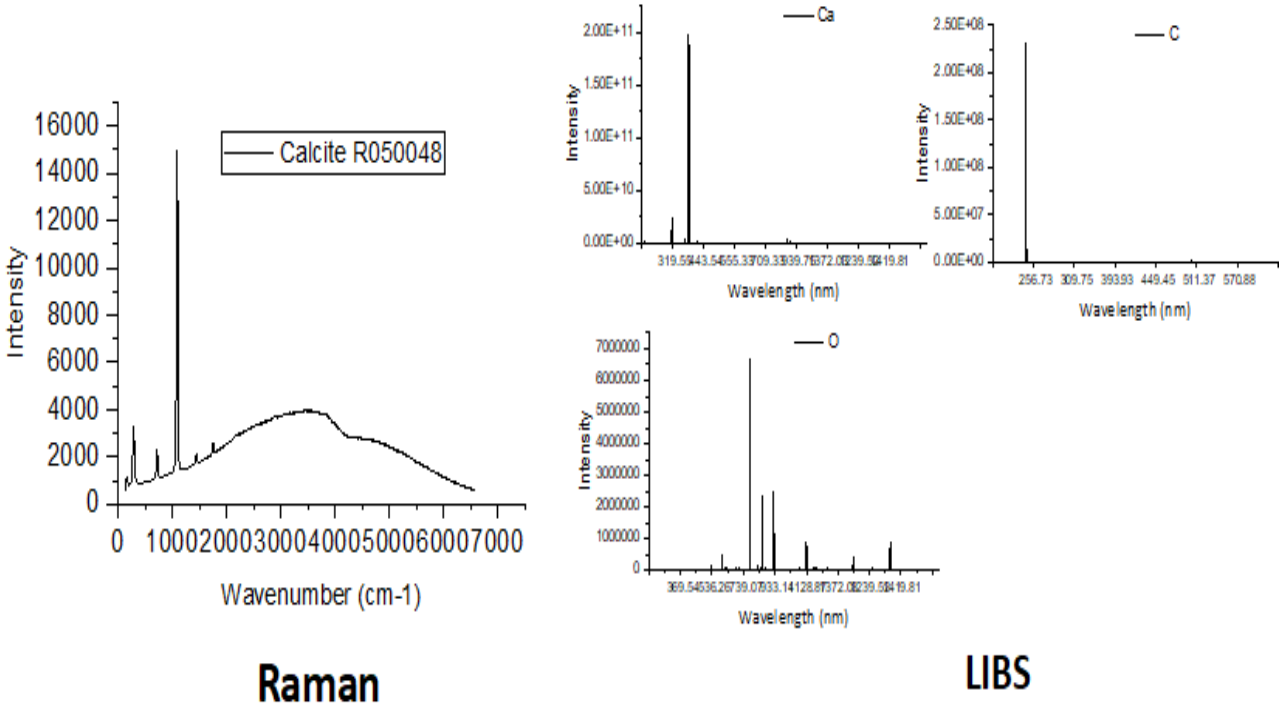

Figure 30: Raman and LIBS spectra of Calcite Origin.

4.2 Discussions

The results clearly indicate that there were variations in several aspects of the spectral peaks for minerals from different sources. Some minerals had peaks within similar ranges of Raman shift but with different intensities. Others had similar intensities but the peaks occurred at different Raman shift ranges. In some cases, both types of differences were observed. These variations can be attributed to issues with line shifts, the presence of impurities, and additional spectral peaks seen in minerals from similar groups. Therefore, a key aspect we considered in this study is the need to correct instrumental issues (such as different technical settings) that may arise from collecting measurements using two different spectroscopies with different lasers simultaneously, before analyzing the data. More information on the LIBS pretreatment can be found in and will be briefly explained. On the other hand, the preprocessing of Raman data specific to this study will be described in detail. To begin with, the entire data set was divided into subsets of spectra, each forming a separate sub-image.

Using advanced data analysis tools like Origin software, the spectral data were accurately visualized, allowing precise peak identification of these minerals. The integration of LIBS and Raman spectroscopy effectively addressed challenges related to impurities, providing a thorough and reliable identification of the mineralogical composition and structural integrity of the samples.

The combined use of LIBS and Raman spectroscopy proved highly effective in identifying key elements such as Fe, Si, and O in minerals like Fe_2SiO_4 (fayalite), Chalcanthite ($Cu(SO_4)•5H_2O$), Calcite ($CaCO_3$), Fayalite (Fe_2SiO_4), Forsterite (Mg_2SiO_4), Gypsum ($Ca(SO_4)•2H_2O$), Halite (NaCl), Nontronite ($Na_{0.3}Fe^{3+}_2(Si,Al)_4O_{10}(OH)_2•nH_2O$), and Quartz ($SiO_2$) using the NIST database for reference. For instance, the Calcite showed a central peak around 1086 cm^{-1}, for R040070 and R050048. Similarly, the olivine fayalite exhibited a central peak around 820 cm^{-1}, detectable in both of our olivine forsterites, reflecting the occasional co-occurrence of these minerals.

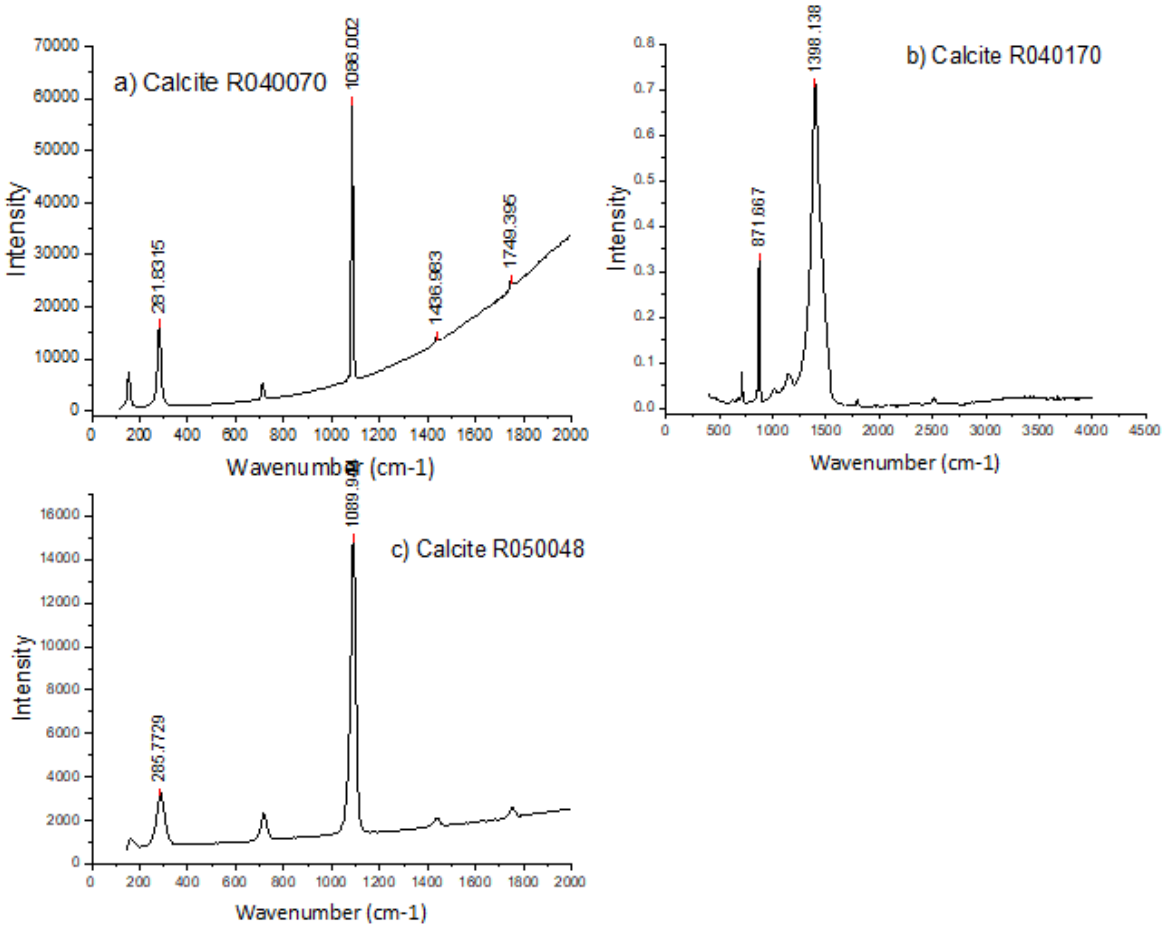

Figure 31: Raman spectra peaks of Calcite

The LIBS technique provided rapid elemental analysis, highlighting strong emission lines for critical elements. For Fe_2SiO_4 (fayalite), significant emission lines for iron (Fe), silicon (Si), and oxygen (O) were identified. Chalcanthite showed strong emission lines for copper (Cu) and sulfur (S), while Calcite exhibited intense lines for calcium (Ca) and carbon (C). Raman spectroscopy further confirmed these findings by identifying the vibrational modes of the minerals. For example, the Raman spectral analysis of Calcite revealed key peaks of the carbonate ion (CO_3^{2-}) at around 1396 cm^{-1}, with additional peaks at 871 cm^{-1} corresponding to bending modes and Gypsum revealed key peaks of the SO_4 at ~1105 cm^{-1}, with additional peaks at 597 cm^{-1}, 669 cm^{-1}. Identification of both SO_4 and Ca supports gypsum.

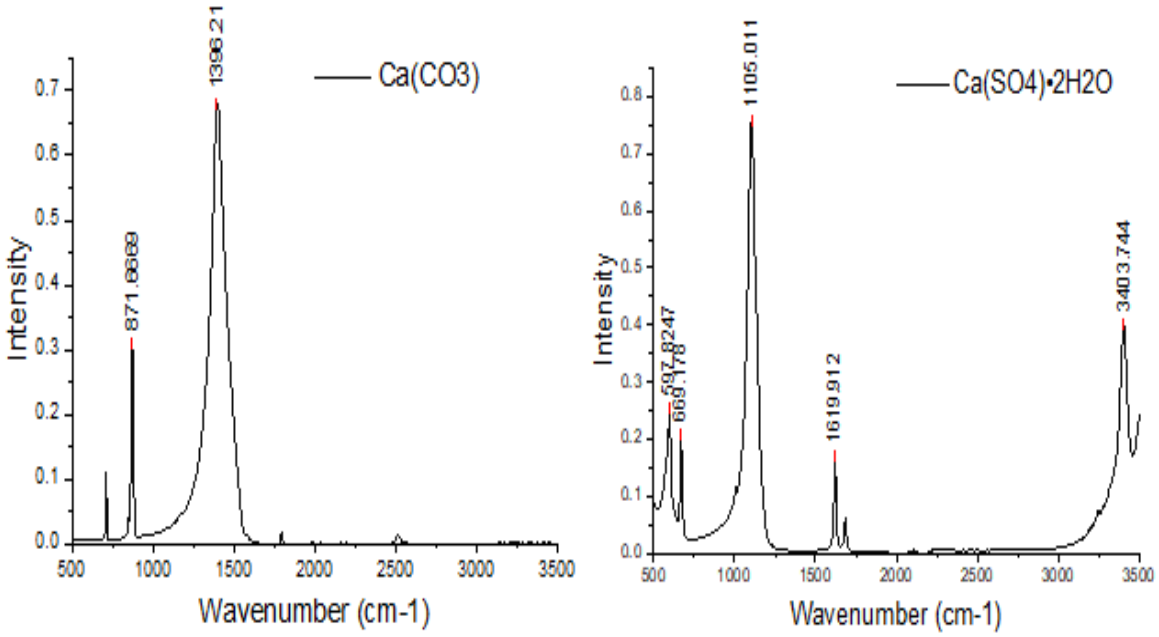

Figure 32: Raman spectra peaks of Calcite and Gypsum Origin.

The Raman spectral analysis of Calcite ($CaCO_3$) was performed by importing the spectral data into Origin software for detailed examination The most intense peak typically appears around 1395 cm^{-1}, representing the symmetric stretching vibration of the CO3 group. Additionally, the bending modes are observed near 871 cm^{-1} and 1435 cm^{-1}. The lattice vibrations of calcium ions (Ca^{2+}) and their interactions with the carbonate groups also contribute to the spectral features, producing weaker bands at lower wavenumbers, typically below 800 cm^{-1}. figure 20 shows the spectra peak analysis of calcite (CaCO3).

The time-gated Raman spectra of the two calcium carbonate minerals, CaSO4 and CaSO4.2H2O in low and high-frequency regions. In the case of gypsum, two sharp bands are observed at 3410 and 3493 cm-1, corresponding to the stretching vibrational mode of water molecule. The two bands show the two types of water molecules in the sample, one attached to sulfate ions by hydrogen bonding, and the other directly linked with the cation (Ca). The strongest Raman band in both cases lies between 1000 and 1030 cm-1.

This combined analytical approach was further validated as many of our samples were confirmed through X-Ray Diffraction (XRD) and chemical analysis methods, ensuring the accuracy of our findings. Overall, the study demonstrates the strength of using both LIBS and Raman spectroscopy together, as they complement each other to provide a detailed and reliable

analysis of mineral samples, enhancing the identification of elements and the understanding of mineral structures.

4.2.1 Element Identification in Minerals Using LIBS and Raman Spectroscopy

The LIBS and Raman spectra peaks obtained for Fayalite (Fe_2SiO_4), Chalcanthite ($CuSO_4 \cdot 5H_2O$), Calcite ($CaCO_3$) and Forsterite (Mg_2SiO_4), is given in Table 1. Peak labels were assigned according to the National Institute of Standards (NIST) LIBS database. LIBS spectra tend to be structurally complex, containing multiple emission lines for most of the elements corresponding to both the primary mineral and other minerals present in the specimen. For instance, the prominent Ca lines fingerprint is partially associated with the calcite (CaCO3). However, the peaks that dominate each of the measured spectra are those of the most abundant divalent and trivalent cations that fit into the layer and interlayer sites of the mineral phase (ie. Mg, Al, Fe, Ca, Na). These peaks are observed in the spectral fingerprints from each specimen with relative strong intensity patterns.

No	Mineral species	LIBS elemental peaks	Raman shift peaks
1	Chalcanthite R050293 ($Cu(SO_4) \cdot 5H_2O$)	Strong Cu Peaks at 271 nm, 357 nm	Strong peaks at 463 cm-1, 985 cm-1
2	Chalcanthite R060102 ($Cu(SO_4) \cdot 5H_2O$)	Strong Cu Peaks at 271 nm, 357 nm	Strong peaks at 982 cm-1, 3196 cm-1
3	Calcite R040070 ($Ca(CO_3)$)	Strong Ca Peaks at 3038 nm, 3107 nm	Strong peaks at 281 cm-1, 1086 cm-1
4	Calcite R040170 ($Ca(CO_3)$)	Strong Ca Peaks at 3038 nm, 3107 nm	Strong peaks at 871 cm-1, 1398 cm-1
5	Calcite R050048 ($Ca(CO_3)$)	Strong Ca Peaks at 3038 nm, 3107 nm	Strong peaks at 285 cm-1, 1089 cm-1
6	Fayalite R100103 ($Fe^{2+}_2(SiO_4)$)	Strong Fe Peaks at 118 nm, 148 nm	Strong peaks at 821 cm-1, 900 cm-1
7	Fayalite R100104 ($Fe^{2+}_2(SiO_4)$)	Strong Fe Peaks at 118 nm, 148 nm	Strong peak at 815 cm-1
8	Fayalite X050076.4 ($Fe^{2+}_2(SiO_4)$)	Strong Fe Peaks at 118 nm, 148 nm	Strong peaks at 814 cm-1, 839 cm-1

9	Fayalite X050077 ($Fe^{2+}_2(SiO_4)$)	Strong Fe Peaks at 118 nm, 148 nm	Strong peak at 820 cm-1
10	Forsterite R040052 ($Mg_2(SiO_4)$)	Strong Fe Peaks at 998 nm, 1013 nm	Strong peaks at 822 cm-1, 855 cm-1
11	Forsterite R050117 ($Mg_2(SiO_4)$)	Strong Fe Peaks at 998 nm, 1013 nm	Strong peaks at 826 cm-1, 857 cm-1
12	Forsterite R060539 ($Mg_2(SiO_4)$)	Strong Fe Peaks at 998 nm, 1013 nm	Strong peaks at 824 cm-1, 855 cm-1
13	Forsterite X050080.4 ($Mg_2(SiO_4)$)	Strong Fe Peaks at 998 nm, 1013 nm	Strong peaks at 824 cm-1, 857 cm-1
14	Forsterite X050081 ($Mg_2(SiO_4)$)	Strong Fe Peaks at 998 nm, 1013 nm	Strong peaks at 823 cm-1, 855 cm-1
15	Forsterite X050090.4 ($Mg_2(SiO_4)$)	Strong Fe Peaks at 998 nm, 1013 nm	Strong peaks at 820 cm-1, 852 cm-1

Table 1: Illustrates LIBS and Raman Spectral peaks of different minerals.

4.2.2 PCA Analysis of LIBS and Raman Spectral Signatures for Mineral Identification

The PCA model built from the LIBS and Raman spectral data of minerals such as Fayalite, Chalcanthite, Calcite, Fayalite, Forsterite, Gypsum, Halite, Nontronite and Quartz was analyzed using Origin software. The data were imported into Origin, where PCA was performed to reveal distinct clustering patterns based on the spectral signatures. The first and second principal components highlighted the variations in mineral compositions, with strong loadings from specific emission lines corresponding to the major elements in each mineral. This analysis effectively demonstrated the ability of LIBS and Raman spectroscopy, combined with advanced data processing in Origin, to differentiate between mineral groups and identify their elemental compositions.

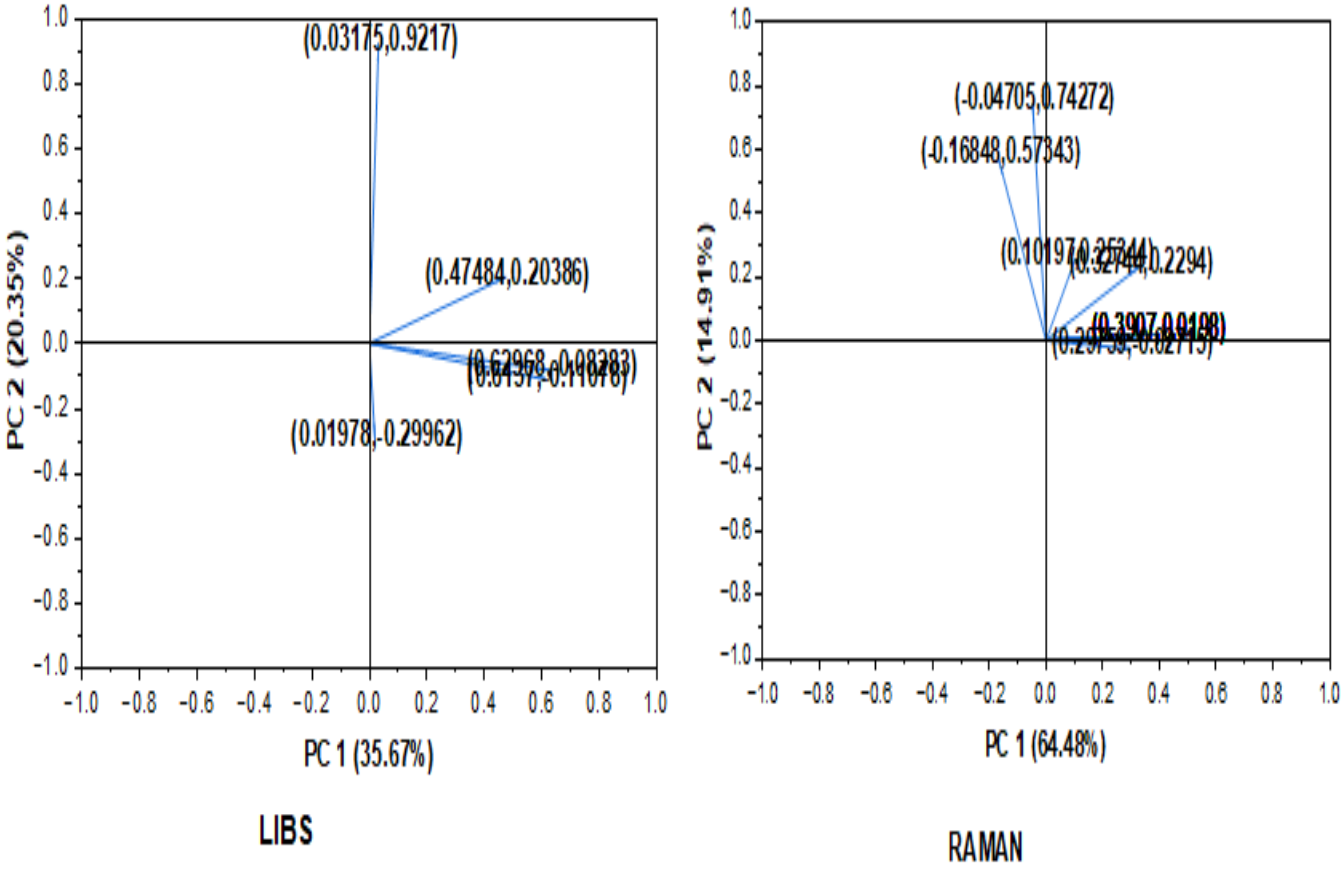

Figure 33: PCA Analysis of LIBS and Raman Spectral of different mineral groups (Source, org)

In the LIBS data scatter plot from the Principal Component Analysis (PCA) shows the distribution of four data points in a two-dimensional space defined by the first two principal components. PC-1 This axis accounts for 35.6% of the variance within the data, indicating it's the most significant pattern of variation. PC-2 accounts for 20.3% of the variance, showing a secondary pattern of variation. The coordinates of the points (0.03175, 0.9217) represent their scores on the principal components.

Also, the imported Raman data were subjected to PCA, scatter plot from a Principal Component Analysis (PCA) shows the horizontal axis (PC-1) accounts for the majority of the variance (64.48%) in the dataset. The vertical axis (PC-2) represents the second principal component, which explains a smaller portion of the variance (14.97%). The four points plotted on the graph are the projections of the original data onto these two principal components. Their coordinates (-0.40705, 0.74272) indicate their position relative to each principal component. Together, PC

1 and PC 2 account for a significant amount of the total variance (79.45%), which means they capture most of the information in the original data. Therefore, this PCA graph helps to visualize and understand the main patterns in the dataset by reducing its dimensionality. It’s particularly useful in spectroscopy for identifying which wavelengths (or other variables) contribute most to the differences between samples.

CHAPTER FIVE

5. CONCLUTIONS AND RECOMMENDATIONS

5.1 Conclusions

The conclusion drawn from this thesis demonstrate that the fused Raman and LIBS spectral analyses of various minerals from different origins yielded distinct and detailed findings regarding their molecular structures and elemental compositions. For Fayalite minerals, each sample exhibited unique Raman spectra with peaks corresponding to specific vibrational modes, reflecting variations in crystallographic orientation, impurities, and structural defects. Forsterite samples showed significant variations in peak positions and intensities, attributable to differences in crystal structure, geological setting, and post-depositional processes. Chalcanthite spectra revealed consistent patterns of peaks indicating similar molecular structures, while slight differences in peak intensities suggested variations in molecular bond concentrations. The results indicate that each mineral species has unique and consistent LIBS elemental peaks and Raman shifts, allowing for clear differentiation. For Chalcanthite ($Cu(SO_4)•5H_2O$), the LIBS analysis consistently identified strong copper peaks at 271 nm and 357 nm across different samples. Gypsum samples exhibited characteristic peaks confirming their identity, with variations in peak intensities pointing to differences in chemical structure or purity. Nontronite spectra showed sharp peaks characteristic of specific molecular bonds, with variations in peak intensities hinting at differences in molecular group concentrations. Quartz samples displayed consistent patterns of sharp peaks, confirming their composition, while slight variations in peak details provided insights into purity and structural differences.

The LIBS spectra complemented the Raman data by identifying the elemental compositions of the minerals. For Chalcanthite, the presence of copper, sulfur, hydrogen, and oxygen was confirmed through distinct spectral lines. Fayalite's elemental analysis indicated strong emissions of iron and silicon, confirming their presence and concentrations in the samples.

By integrating the LIBS and Raman spectral data, comprehensive profiles were generated, enhancing the identification and characterization of the minerals. For instance, in the case of

Calcite, the Raman spectra provided detailed insights into molecular vibrations and lattice structures, while the LIBS spectra confirmed the elemental composition of calcium, carbon, and oxygen. This combined analysis validated the presence of carbonate ions and the crystalline structure of calcite, demonstrating the effectiveness of fusing these two spectroscopic techniques to achieve a more thorough understanding of mineral properties. The Raman shifts showed strong peaks around 463 cm^{-1}, 982 cm^{-1}, and 3196 cm^{-1}, facilitating the identification of chalcanthite samples. Calcite ($Ca(CO_3)$) samples were characterized by strong calcium peaks at 3038 nm and 3107 nm in the LIBS spectra, with Raman analysis revealing peaks at 281 cm^{-1}, 1086 cm^{-1}, 871 cm^{-1}, and 1398 cm^{-1}, confirming the presence of calcite. Fayalite ($Fe^{+}_{2}{}_{2}(SiO_4)$) samples exhibited strong iron peaks at 118 nm and 148 nm in the LIBS spectra, with Raman spectra showing peaks around 814 cm^{-1} to 839 cm^{-1}, indicative of the fayalite structure and composition. Forsterite ($Mg_2(SiO_4)$) consistently showed strong iron peaks at 998 nm and 1013 nm in the LIBS analysis, with Raman spectra indicating peaks around 820 cm^{-1} to 857 cm^{-1}, characteristic of forsterite.

Multivariate Analysis (MVA) tools were applied separately to LIBS and Raman data and to a combined dataset of both. The primary objective was to identify different samples and mixtures, utilizing various strategies to compare and evaluate LIBS and Raman data through Principal Component Analysis (PCA) and Partial Least Squares (PLS) models.

A future target is to estimate the lithium and boron contents within the individual phases, as these elements could be of diagnostic relevance for proxies of mineral deposits. Moreover, for this task, the proposed combination of methods could help.

5.2 Recommendations

Future researchers and students should prioritize addressing potential instrumental issues that arise when using LIBS and Raman spectroscopy simultaneously. Ensuring proper calibration and correction before data analysis is essential to obtain accurate results. Efficient preprocessing of data, such as dividing it into subsets, can significantly enhance computational efficiency and should be adopted in future studies. Advanced software tools like Origin should be utilized for precise peak identification and comprehensive spectral analysis. Combining LIBS and Raman spectroscopy, along with validating findings through X-Ray Diffraction (XRD) and chemical analysis, can provide a robust and reliable analysis of mineral samples. Researchers should also consider the presence of impurities and potential line shifts when interpreting spectral data. Expanding the analysis to include a broader range of minerals will further enhance understanding of mineral compositions and structures. Detailed documentation of methodologies and results is crucial for transparency and reproducibility. Educational programs should emphasize practical training in these advanced analytical techniques, preparing students for future research. Interdisciplinary collaboration should be encouraged to leverage the strengths of different scientific domains. In our country this combined analytical approach can be particularly beneficial. This can lead to better resource management, improved economic development, and sustainable exploitation of natural resources. By building local expertise in these advanced analytical methods, Ethiopia can strengthen its research infrastructure and contribute to global scientific advancements in mineralogy.

REFERENCES

Boss, C. B., & Fredeen, K. J. (1997). Concepts, Instrumentation and Techniques in Inductively Coupled Plasma Optical Emission Spectrometry. PerkinElmer.

Clark, R. N. (1999). Spectroscopy of Rocks and Minerals, and Principles of Spectroscopy. In Manual of Remote Sensing. John Wiley & Sons.

Colao, F., Fantoni, R., Lazic, V., Paolini, A., & Spizz chino, V. (2004). "LIBS experimental and theoretical approach to the study of mock lunar rocks." Spectrochemical Acta Part B: Atomic Spectroscopy, 59(10-11), 1237-1246.

Cremers, D. A., & Radziemski, L. J. (Eds.). (2013). Handbook of Laser-Induced Breakdown Spectroscopy. John Wiley & Sons.

Cremers, D. A., and Radziemski, L. J. (Eds.). (2006). Handbook of Laser-Induced Breakdown Spectroscopy. John Wiley & Sons.

Dubessy, J., Caumont, M. C., & Rull, F. (Eds.). (2012). Raman Spectroscopy Applied to Earth Sciences and Cultural Heritage. EMU Notes in Mineralogy, Volume 12.

Ferraro, J. R., Nakamoto, K., & Brown, C. W. (2003). Introductory Raman Spectroscopy. Academic Press.

Forni, O., Clegg, S., Maurice, S., Wiens, R. C., Gasnault, O., Mangold, N., ... & Lasue, J. (2013). ChemCam passive reflectance spectroscopy of surface materials at the Curiosity landing site, Mars. Icarus, 224(2), 307-325.

Gaft, M., Nagli, L., & Modiano, H. (2005). "Laser-induced breakdown spectroscopy for online multi-element analysis of minerals." Spectrochemical Acta Part B: Atomic Spectroscopy, 60(8), 1125-1137.

Gaft, M., Nagli, L., & Panczer, G. (2012). "Data fusion in spectroscopy: A review of methods and applications." Spectrochemical Acta Part B: Atomic Spectroscopy, 71-72, 1-22.

Geladi, P., & Kowalski, B. R. (1986). Partial least-squares regression: a tutorial. Analytica Chemical Acta, 185, 1-17.

Hahn, D. W., & Omenetto, N. (2010). "Laser-induced breakdown spectroscopy (LIBS), part I: Review of basic diagnostics and plasma–particle interactions: Still-challenging issues within the analytical plasma community." *Applied Spectroscopy*, 64(12), 335A-366A.

Harmon, R. S., Russo, R. E., & Hark, R. R. (2013). "Application of laser-induced breakdown spectroscopy for geochemical and environmental analysis: A comprehensive review." Spectrochemical Acta Part B: Atomic Spectroscopy, 87, 11-26.

Hilbk-Kortenbruck, F., Noll, R., & Connemann, S. (2001). "Laser-induced breakdown spectroscopy for process control in the steel industry." Spectrochemical Acta Part B: Atomic Spectroscopy, 56(6), 933-945.

Hoehse, M. (2012). "Data fusion approaches for laser-induced breakdown and Raman spectroscopies." *Analytical and Bioanalytical Chemistry*, 403(9), 2475-2482.

Hollas, J. M. (2004). Modern Spectroscopy. John Wiley & Sons.

Kerr, P. F. (1959). Raman Spectroscopy of Minerals and Inorganic Compounds. The Journal of Chemical Physics, 31(2), 567.

Kessler, H. (2007). Partial Least Squares Regression: A Tutorial. Analytical Chemistry, 79(10), 3901-3908.

Long, D. A. (2002). The Raman Effect: A Unified Treatment of the Theory of Raman Scattering by Molecules. John Wiley & Sons.

McCreery, R. L. (2000). Raman Spectroscopy for Chemical Analysis. John Wiley & Sons.

Moros, J., Soriano-Disla, J. M., & Laserna, J. J. (2018). "Combined Raman and LIBS for the identification of minerals relevant to Mars exploration: A data fusion approach." Spectrochemical Acta Part B: Atomic Spectroscopy, 143, 31-40.

Pieters, C. M., & Englert, P. A. J. (Eds.). (1993). Remote Geochemical Analysis: Elemental and Mineralogical Composition. Cambridge University Press.

Raman, C. V., & Krishnan, K. S. (1928). "A new type of secondary radiation." Nature, 121, 501-502.

Rayleigh, L. (1899). "On the light from the sky, its polarization and colour." Philosophical Magazine, 47(287), 375-384.

Schröder, S., & Wiens, R. C. (2019). "Laser-induced breakdown spectroscopy in geosciences—a review of its application and the future." Spectrochemical Acta Part B: Atomic Spectroscopy, 161, 105692.

Senesi, G. S., & Senesi, N. (2014). "Laser-Induced Breakdown Spectroscopy (LIBS) to Measure Soil Carbonate Content." Soil Science Society of America Journal, 78(4), 1236-1244.

Sharma, S. K., Misra, A. K., & Lucey, P. G. (2006). "Combined remote LIBS and Raman spectroscopy at 8.6 m for analysis of minerals, rocks, and soils under supercritical CO2 relevant to Mars." Applied Spectroscopy, 60(7), 744-750.

Singh, J. P., & Thakur, S. N. (Eds.). (2007). Laser-Induced Breakdown Spectroscopy. Elsevier.

Smith, E., & Dent, G. (2005). Modern Raman Spectroscopy: A Practical Approach. John Wiley & Sons.

Surmick, D. M., Leahy-Hoppa, M. R., & Malenfant, J. (2016). "Advances in Laser-Induced Breakdown Spectroscopy for Biological, Chemical, and Environmental Applications." Appl Spectroscopy Rev, 51(1), 22-50.

Tyndall, J. (1869). "On the blue color of the sky, the polarization of skylight, and on the polarization of light by cloudy matter generally." Proceedings of the Royal Society of London, 17, 223-233.

Welz, B., & Sperling, M. (1999). Atomic Absorption Spectrometry. Wiley-VCH.

Wiens, R. C., Maurice, S., & Perez, R. (2017). "The Super Cam remote sensing instrument suite for Mars 2020." Spectroscopy, 32(2), 50-55.

Wilhelms, D. E. (1993). To a Rocky Moon: A Geologist's History of Lunar Exploration. University of Arizona Press.